Metabolic basis of the astrocyte-synapse interaction governs dopaminergic-motor connection

Yanru Xu[1,2,3], Piaoping Kong[1,2,3], Mengqi Wang[2], Yanyun Mao[2], Zhiguo Ma[1,2]*

[1]Department of Neurobiology, Affiliated Mental Health Center and Hangzhou Seventh People's Hospital, School of Brain Science and Brain Medicine, Zhejiang University School of Medicine, Hangzhou, China

[2]Liangzhu Laboratory, MOE Frontier Science Center for Brain Science and Brain-machine Integration, State Key Laboratory of Brain-machine Intelligence, NHC and CAMS Key Laboratory of Medical Neurobiology, Zhejiang University, Hangzhou, China

[3]These authors contributed equally

*Corresponding to: Zhiguo Ma

Email: zgma@zju.edu.cn

Author Contributions: Conceptualization: Z.G.M.; Methodology: Z.G.M., Y.R.X.; Investigation: Z.G.M., Y.R.X., P.P.K., M.Q.W., Y.Y.M.; Validation: Z.G.M., Y.R.X., M.Q.W.; Visualization: Z.G.M., Y.R.X.; Formal analysis: Z.G.M., Y.R.X.; Data curation: Z.G.M., Y.R.X.; Resources: Z.G.M.; Software: Z.G.M.; Project administration: Z.G.M.; Funding acquisition: Z.G.M.; Supervision: Z.G.M.; Writing – original draft: Z.G.M., Y.R.X.; Writing – review & editing: Z.G.M.

Competing Interest Statement: Authors declare that they have no competing interests

Abstract

Perisynaptic astrocyte processes are constitutive attachments of synapses in the central nervous system. However, the molecular mechanisms that control perisynaptic astrocyte ensheathment and their implications in the wiring of neural circuits remain unclear. Here, we report that glycolysis controls astrocyte-synapse contact. In the *Drosophila* larval dopaminergic (DAergic) circuit, blocking astrocyte glycolysis stimulated perisynaptic ensheathment by attenuating astrocyte-to-DAergic neuron neuroligin 2-neurexin 1 signaling. As a result, the larvae executed more reorientation actions during locomotion. At the circuit level, behavioral alterations were found to arise from increased DAergic neuronal synaptogenesis and DAergic-motor connection. Our research uncovers an ancient metabolic basis that determines perisynaptic astrocyte ensheathment abundance through a conserved neuroligin-neurexin signaling pathway and demonstrates the role of astrocyte glycolysis in controlling DAergic-motor circuit assembly and function.

Keywords: perisynaptic astrocyte processes; astrocyte; glycolysis; dopaminergic circuit; neuroligin-neurexin signaling

Main Text

Introduction

Astrocytes have a complex morphology with dense branches ensheathing many synapses[1–3]. Consequently, perisynaptic astrocyte processes and synapses are positioned in immediate vicinity for astrocyte-synapse interaction. Astrocyte-synapse contact is modulated by synaptic activity and several cell-cell communication pathways such as cell-adhesion signaling[4–14].

Astrocytes are key non-neuronal cells that interact with the DAergic system[15–17]. The DAergic system comprises many subcircuits with patterned synaptic connectivity, each of which controls specific actions[18,19]. Imbalances in DAergic subcircuit connectivity are associated with both motor and non-motor deficits in neurodevelopmental disorders such as autism and schizophrenia[20–24]. Perisynaptic astrocyte processes regulate neurotransmission at DAergic synapses[25–28]; however, whether they contribute to patterning synaptic connection of developing DAergic subcircuits is unknown.

Neuroligins (Nlgs) and neurexins (Nrxs) are ligand-receptor, cell-adhesion molecules (CAMs) responsible for regulating synapse assembly and function[29–32]. The Nlg-Nrx signaling was traditionally viewed as a neuron-to-neuron communication pathway. For instance, postsynaptic Nlg2 and Nlg3 instruct DAergic presynapse organization[33,34], and conditional

knockouts of all Nrxs in DAergic neurons cause disproportionate co-transmission at DAergic synapses[35]. However, recent findings have provided new insights into the intercellular modalities of Nlg-Nrx signaling. Nonneuronal cells in the central nervous system (CNS), such as astrocytes, also express Nlgs[36,37]. In fact, astrocyte-neuronal Nlg-Nrx signaling is critical for excitation/inhibition balance and neural plasticity and regulates synaptogenesis in a circuit-specific manner [8,38]. It is crucial to redefine the role of Nlg-Nrx signaling in the wiring of DAergic circuits; however, the question of how astrocyte-neuronal Nlg-Nrx signaling is regulated remains unclear.

Astocytes are efficient at glycolysis and supply the brain with glycolytic intermediates essential for neural biomass growth including synaptogenesis[39], and the maintenance of neuronal activity[40]. Consistent with the established functions of vertebrate astrocytes, studies in *Drosophila* have demonstrated that astrocyte ablation impairs cholinergic synaptogenesis in the pupal antennal lobes[41], while deficits in glial glycolysis lead to neuronal death in adult flies[42]. However, it remains to be elucidated whether the astrocyte-neuronal communication pathways, specifically Nlg-Nrx signaling and glycolysis, converge to regulate synaptogenesis and the precise wiring of neural circuit.

Here, using a previously unexplored *Drosophila* model addressing astrocyte-DAergic synapse interactions, we show the metabolic regulation of astrocyte-neuronal Nlg-Nrx signaling by glycolysis in controlling perisynaptic astrocyte ensheathment, DAergic-motor subcircuit wiring, and motor function. Our findings advance the understanding of astrocyte-synaptic mechanisms underlying the metabolic modulation of motor control by dopamine.

Results

Astrocyte ensheathment of DAergic synapses

First, to trace perisynaptic ensheathment by astrocytes in proximity of DAergic synapses (hereafter referred to as PEAPODs), we expressed membrane-tethered split GFP (spGFP) fragments, CD4-spGFP$^{1-10}$ and CD4-spGFP^{11}, in astrocytes and DAergic neurons, respectively, in *Drosophila* larvae, using two binary expression systems, namely Gal4/UAS and LexA/lexAop (Fig. S1A)[15,43–46]. As several previous studies have modeled astrocyte interactions with the monoaminergic, motor, and GABAergic systems in the larval ventral nerve cord (VNC), we also chose to focus on the VNC[15,38,41]. Using GFP reconstitution, we identified many astrocyte-DAergic neuronal contact sites, which disperse along DAergic neuronal processes and show regional variations in intensity across the VNC and brain (Fig. S1B). Many of them resembled synaptic boutons and adjoined or contained core active zone protein Bruchpilot (Brp), indicative

100 of perisynaptic astrocyte ensheathment of DAergic synapses (i.e., PEAPODs) (Fig. 1A;
101 Supplemental video S1). This differs from larval glutamatergic circuit where astrocyte-synapse
102 contact is rare[47]. To quantitate the astrocyte-DAergic synapse association, we examined
103 PEAPODs and DAergic neurons expressing the presynaptic marker Bruchpilot^{short}-mStraw
104 (Brp.S-mStraw) at single-cell resolution using FLP-out[44,48]. As a result, we found that 87.5% ±
105 0.55% of Brp.S-mStraw puncta were associated with PEAPODs in the VNC, and the number
106 dropped to 41.9% ± 1.07% in the brain (Figs. 1B–1D; Fig. S1C).

107 Neuronal activity remodels astrocyte-synapse contact, and DAergic neurons
108 spontaneously fire in bursts[15,49]. To determine how PEAPODs reorganize during DAergic
109 neuronal activation, we performed dual-color live imaging of PEAPODs and measured the
110 activity of DAergic neurons using the membrane-tethered Ca^{2+} indicator mR-GECO1 (Fig. S1D;
111 Supplemental video S2)[50]. We recorded active DAergic neuronal branches that appeared to be
112 transversal projections from vmTH neurons[51]. Spontaneous DAergic neuronal bursting plotted
113 a bell-shaped Ca^{2+} curve, for which we named three phases: rising, sustaining, and decay
114 periods (RP, SP, and DP, respectively) (Fig. 1E). The RP and DP Ca^{2+} levels (135.2% ± 12.21%
115 vs. 152.1% ± 9.71%, maximum normalized difference in fluorescence levels between any given
116 time point and the basal state [dF/F]) were similar and dramatically lower than those of the SP
117 (512.1% ± 31.21%, maximum dF/F) (Fig. 1F). PEAPODs presented a multiple-peak response
118 during DAergic neuronal burst firing (Fig. 1E). In contrast to the bell-shaped DAergic neuronal
119 Ca^{2+} activity with a pair of symmetrical RP, DP shoulders, and an SP peak, the PEAPODs
120 exhibited equivalent increases in intensity during the RP, SP, and DP (9.2% ± 0.97%, 11.9% ±
121 1.85%, and 12.9% ± 1.94%, respectively; maximum dF/F) (Figs. 1G and 1H), before returning
122 to baseline. Therefore, spontaneous DAergic neuronal activity is not sufficient to stabilize
123 temporarily enhanced PEAPODs. Thermogenetic activation of DAergic neurons for 30 min
124 using the cation channel TrpA1 did not change the intensity of the PEAPODs (Fig. 1I). Finally,
125 we inhibited DAergic neurons by hyperpolarizing the membrane potential using the potassium
126 inwardly rectifying channel mKcnj2 or by blocking synaptic transmission with the tetanus toxin
127 TNT-G, with none showing significantly altered PEAPODs intensity (Fig. 1I). Taken together,
128 these results suggest that astrocyte-DAergic synapse contact is transiently stimulated during
129 spontaneous DAergic neuronal burst firing, but that DAergic neuronal activity is dispensable for
130 PEAPODs.

131

132 **Astrocytes determine the abundance of PEAPODs via glycolysis**

133

134 Glycolysis breaks down one glucose molecule into two molecules of pyruvate (Fig. 2A).
135 Vertebrate astrocytes exhibit high glycolytic activity[52,53], and glial glycolysis has been shown
136 critical for neuronal survival in adult flies[42]. We found that the knockdown (KD) of glycolytic
137 genes by RNAi, including *phosphofructokinase* (*pfk*), *enolase* (*eno*), and *pyruvate kinase* (*pyk*),
138 in astrocytes increased the intensity and number of PEAPODs by several folds: *pfk* RNAi (e.g.,

139 5.6 ± 0.12, 2.2 ± 0.02), *eno* RNAi (e.g., 7.0 ± 0.18, 2.4 ± 0.05), and *pyk* RNAi (e.g., 5.8 ± 0.10,
140 2.0 ± 0.02) (intensity, number; fold change). In addition, knocking down these genes in
141 astrocytes caused many PEAPODs to enlarge hundreds of times in volume (Figs. 2B–2E, S2A–
142 S2D).

143 Pyk is the final-step, rate-limiting enzyme that converts phosphoenolpyruvate to pyruvate
144 during glycolysis. Anti-Pyk antibody staining showed that Pyk was enriched in astrocytes (Fig.
145 2F), and astrocyte *pyk* KD diminished its expression (Fig. 2G). Next, we recovered two *pyk*
146 alleles by CRISPR-Cas9 mutagenesis[54–57], pyk^{11} and pyk^{7}, which carried 1-bp (pyk^{11}) and 17-
147 bp (pyk^{7}) frameshift deletions in the largest *pyk* exon, respectively (Fig. S3A). Pyk expression
148 was severely reduced in the mutants (e.g., 27.7% ± 4.68% remained in $pyk^{11/7}$) (Figs. S3B and
149 S3C), which caused the mutants to die at the 2nd instar larval stage. Similar to astrocyte *pyk*
150 RNAi, *pyk* mutations also increased PEAPODs (Figs. 2H–2K). In conclusion, astrocytes
151 determine the PEAPODs abundance by glycolysis.

152

153 **Glycolysis-deficient astrocytes promote DAergic neuron synaptogenesis**

154

155 *Drosophila* astrocytes exhibit a striking homology with their vertebrate counterparts in
156 morphology and function. For example, astrocytes, characteristic of sophisticated bushy
157 processes in both species, infiltrate the neuropile where they ensheath synapses and play a
158 key role in synaptogenesis[41,58–65]. We labeled astrocytes with membrane-tethered GFP (i.e.,
159 mCD8-GFP) and observed equivalent amounts of astrocytes and normal neuropile infiltration
160 in the *pyk* mutant compared to the control (Figs. 3A and 3B). Using anti-Brp antibody staining,
161 we detected similar levels of Brp in the *pyk* mutant compared to the control, suggesting that
162 overall CNS synaptogenesis is not affected by glycolysis deficiency (Fig. 3C). To examine
163 astrocyte morphology, we conducted mosaic analysis with a repressible cell marker (MARCM)
164 to label single astrocytes[66]. We found *pyk* mutant astrocytes formed thick branchlets and
165 radiated out to the size of control (Figs. 3D and 3E).

166 We showed that astrocyte glycolysis deficiency increased the abundance of PEAPODs.
167 Therefore, we next examined whether DAergic synaptogenesis was altered in turn. To this end,
168 we specifically labeled endogenous Brp in DAergic neurons with a flip-out cassette,
169 *Brp>FSF>GFP*, using STaR[67]. We created a $lexAop2\text{-}pyk^{RNAi}$ transgenic line to knock down *pyk*
170 in astrocytes (Fig. S3D). Astrocyte *pyk* KD using the LexA/lexAop system showed identical
171 PEAPODs enhancement phenotypes (Figs. S3E–S3G). We observed that astrocyte *pyk* KD
172 increased endogenous Brp expression in DAergic neurons to 123.8% ± 1.75% of the control
173 (Figs. 3F and 3G), while the overall CNS synaptogenesis remained unchanged (α-Brp and
174 transmission electron microscopy; Figs. 3H and 3I). Thus, astrocyte glycolysis deficiency
175 promotes DAergic neuron synaptogenesis. However, we do not rule out that non-DAergic
176 synaptogenesis is also altered by astrocyte glycolysis deficiency. It is unlikely that Brp

177 stimulates PEAPODs because the *brp* KD in DAergic neurons enhances PEAPODs (Figs.
178 S4A–S4C).

179

180 **Astrocyte glycolysis deficiency leads to biased DAergic circuit wiring**

181

182 We demonstrated that astrocyte glycolysis deficiency increased PEAPODs and DAergic neuron
183 synaptogenesis. However, whether this had a significant effect on DAergic circuit assembly
184 remains an open question. In *Drosophila*, postsynaptic connections with the DAergic system
185 remain largely unknown, particularly those in the larval VNC. To address this issue, we profiled
186 postsynaptic partners wired to DAergic neurons in the larval CNS. Briefly, we labeled the
187 postsynaptic cells with mtdTomato by transsynaptic tracing (i.e., *trans*-Tango) and pooled
188 mtdTomato$^+$ cells using fluorescence-activated cell sorting (FACS)[68,69]. Subsequently, we
189 performed single-cell RNA sequencing (scRNA-seq) and cell type annotation to identify the
190 cohort-based postsynaptic connectome of the larval DAergic system (Fig. 4A).

191 We dissected 50 CNSs each from the control and astrocyte *pyk* KD larvae, ultimately
192 obtaining 11815 and 13327 (control vs. astrocyte *pyk* KD) mtdTomato$^+$ cells, respectively,
193 which were sequenced. The higher yield of mtdTomato$^+$ cells from astrocyte *pyk* KD is in line
194 with our observation that KD led to stronger mtdTomato expression by *trans*-Tango, which
195 suggests that DAergic neurons make more postsynaptic connections (Figs. S4D and S4E).
196 These individual cells were grouped into 20 clusters in uniform manifold approximation and
197 projection (uMAP) analysis (Fig. S5A). *nsyb*$^+$*para*$^+$ cells were selected as mature neurons[70,71],
198 which accounted for 47.3% (control) and 54.3% (astrocyte *pyk* KD) of all cells sequenced (Figs.
199 S5B–S5E). The mature neurons re-clustered in 12 groups (Fig. 4B). Next, using unique marker
200 genes[71,72], we performed cell type annotation and defined eight mature neuron populations
201 (Figs. S5F, S5G, and S6A–S6J; Table S1)[73]. Our annotation is of high accuracy: for instance,
202 93.9% *twit*$^+$ motor neurons (MNs) can be sorted into known MN subclasses with an additional
203 marker gene, e.g., 53.6% glutamatergic type I (*vglut*$^+$), 18.2% octopaminergic type II (*tβh*$^+$), and
204 22.1% neuropeptidergic type III (*phm*$^+$) (Table S2)[74,75]. Moreover, excitatory/inhibitory
205 populations appeared to be mutually exclusive in the uMAP analysis, e.g., glutamatergic vs.
206 GABAergic populations (Figs. S6B vs. S6C) and GABAergic vs. cholinergic populations (Figs.
207 S6C vs. S6D). We compared the cell numbers of each population in the control and astrocyte
208 *pyk* KD, with the astrocyte *pyk* KD often outnumbering the controls. The MNs, gathered in
209 cluster 12, had the highest fold change (>2.6), followed by the neuropeptidergic neurons (>1.5)
210 and DAergic neurons (>1.4) (Figs. 4C–4E). Therefore, enhanced DAergic synaptogenesis
211 caused by astrocyte glycolysis deficiency indeed gives rise to more postsynaptic connections.
212 Taken together, our data demonstrate that astrocyte glycolysis deficiency leads to biased
213 DAergic circuit wiring.

214

Biased DAergic-motor wiring alters motor output

Dopamine modulates motor circuit dynamics[76–80]. To examine whether biased DAergic-motor wiring alters motor output, we tracked and analyzed *Drosophila* larval locomotion using the frustrated total internal reflection (FTIR)-based imaging method[81,82]. This larval behavior manifests as a series of active forward, as well as a few backward, crawling (i.e., peristalsis) actions interrupted by stereotyped reorientation attempts (i.e., pauses and sweeps) (Fig. 5A)[83–85]. Compared to the controls, the astrocyte *pyk* KD larvae travelled in densely branched trajectories (Fig. 5B). They increased the likelihood of pausing (e.g., 16.4% ± 0.22% vs. 6.0% ± 0.27%, astrocyte *pyk* KD vs. ctrl) and sweeping (e.g., 16.8% ± 0.23% vs. 5.9% ± 0.26%, astrocyte *pyk* KD vs. ctrl) without changing bending strength (Figs. 5C–5E). During the peristaltic sessions, the RNAi larvae attained a higher maximum speed (e.g., 2.7 mm/s ± 0.04 mm/s vs. 1.9 mm/s ± 0.02 mm/s, astrocyte *pyk* KD vs. ctrl) and maintained similar peristalsis efficiency and frequency (Figs. 5F–5H).

Glycolysis controls the astrocyte-DAergic synapse interaction by Nlg2-Nrx1 signaling

It remains to be determined how astrocytes transduce the glycolytic event into a means of cell-cell communication guiding astrocyte-DAergic synapse interaction. CAMs such as Nlgs and Nrxs modulate astrocyte-synapse contact and synaptogenesis[8,38]. We assayed the effect of KDs of Nlgs and Nrxs on PEAPODs by RNAi and found that both astrocyte *nlg2* KD and DAergic neuron *nrx1* KD increased PEAPODs, e.g., astrocyte *nlg2* RNAi (5.2 ± 0.08, 2.9 ± 0.04) and DAergic neuron *nrx1* RNAi (2.4 ± 0.04, 1.9 ± 0.03) (intensity, number; fold change) (Figs. 6A–6H). In addition, *nrx1* RNAi in DAergic neurons enhanced synaptogenesis to 112.8% ± 0.63% of the control (Figs. 6I–6J). In summary, these data suggest that astrocyte glycolysis and astrocyte-DAergic neuronal Nlg2-Nrx1 signaling are somehow in the same pathway responsible for controlling PEAPODs and DAergic synaptogenesis. Using anti-Nlg2 antibody staining, we observed massive intra-astrocyte membranous Nlg2 bodies in the *pyk* mutant (Figs. 6K and 6L). The Nlg2 bodies were decorated with the endoplasmic reticulum (ER) luminal reporter GFP-KDEL, indicating that Nlg2 ER exit fails in *pyk* mutant astrocytes. Taken together, our findings support the notion that astrocyte glycolysis enables astrocyte-to-DAergic neuron Nlg2-Nrx1 signaling to restrict astrocyte-DAergic synapse contact and DAergic synaptogenesis.

Discussion

Our data indicate a metabolic basis for perisynaptic astrocyte ensheathment. Glycolysis is critical for proper Nlg2 trafficking in astrocytes, and astrocyte-DAergic neuronal Nlg2-Nrx1

signaling relies on astrocyte glycolysis. This metabolic signaling axis (glycolysis/Nlg2-Nrx1) restricts perisynaptic astrocyte ensheathment; once it fails during development, the astrocyte-synapse contact rises and DAergic neurons increase synaptogenesis and their synaptic connection with motor neurons.

Nlg family proteins are transported to the cell surface where they bind Nrx receptors[86]. Nlgs contain many amino acid residues involved in N- and O-linked glycosylation[87,88]. Posttranslational glycosylation is crucial for Nlgs on their way to activating Nrxs, from protein folding to surface trafficking, as well as Nrx binding[89,90]. Autism-associated mutations of several *nlg* genes lead to differentially glycosylated Nlg proteins and their retention at the ER[91–93]. In this study, we showed that Nlg2 (mammalian Nlg1 homolog) is sequestered at the ER in glycolysis-deficient astrocytes. Modulations in glycolytic flux alter protein glycosylation outcomes[94–99]. Taken together, our findings suggest a similar mechanism for Nlg2 retention in the ER owing to aberrant glycosylation in glycolysis-deficient astrocytes. As a result, perisynaptic astrocyte ensheathment increases at DAergic synapses.

In terms of how perisynaptic astrocyte ensheathment abundance is relevant to synaptogenesis, previous studies have shown that astrocyte Nlg2 knockout reduced both perisynaptic astrocyte contact and glutamatergic synaptogenesis[8]. Additionally, the depletion of neuronal cell adhesion molecule (NRCAM) in astrocytes enhances astrocyte-synapse adhesion but decreases GABAergic synaptogenesis[10]. In contrast, our data indicate that astrocyte Nlg2 deficiency increases both perisynaptic astrocyte ensheathment and DAergic synaptogenesis. In summary, these findings suggest that perisynaptic astrocyte ensheathment abundance is a proxy for measuring astrocyte-synapse interaction but is not directly or inversely proportionally linked to synaptogenesis. Complex contact-mediated astrocyte-synaptic mechanisms regulate synaptogenesis, which involve the heterogeneity of synapses and neural circuits.

We mapped cohort-based postsynaptic connectomes of the *Drosophila* larval DAergic system using transsynaptic tracing, scRNA-seq, and cell type annotation. The connectomes comprise several heterogeneous populations. Most of the populations were annotated using defined marker genes associated with neurotransmitter types but not behavioral signatures. Therefore, our current analyses have a limited depth with regard to analyzing DAergic subcircuits associated with specific behaviors. However, the connectomes we constructed are valuable reference landscapes for DAergic subcircuit mapping when unique marker genes emerge in the midst of investigating dopamine signaling during *Drosophila* development. For instance, in this study, we observed a single molecularly defined population, the MNs, designated for locomotion. We found that astrocyte glycolysis deficiency led to more than double the number of MNs in synaptic connection with the DAergic system. Notably, astrocyte Nlg2 depletion extends the critical window of *Drosophila* larval motor circuit, which induces long-term changes in motor circuit wiring and behavior during development[38]. Similarly, we showed that astrocyte glycolysis deficiency causes astrocyte-neuronal Nlg2-Nrx1 signaling to

291 fail and enhances DAergic synaptogenesis. Taken together, the data suggest that *Drosophila*
292 astrocytes control the wiring of DAergic circuit among others by glycolysis. DAergic neurons
293 start to appear as early as embryogenesis stage 14, before the motor critical window closes
294 normally, beginning a few hours after larval hatching[38,100]. It remains unclear whether larval
295 motor circuit plasticity plays a role in favoring DAergic-motor connection due to astrocyte
296 glycolysis deficiency.

297 Primitive glycolysis is a fundamental metabolic process in astrocytes[101]. Our study opens
298 new opportunities for uncovering the neurometabolic implications in neural circuit connectivity,
299 particularly of the DAergic system.

300

301

302 **Acknowledgements**

303

304 This work was supported by National Excellent Young Scientists Fund (Overseas) and in part
305 by Non-profit Central Research Institute Fund of Chinese Academy of Medical Sciences (2023-
306 PT310-01). We thank the core facilities of Liangzhu Laboratory and the core facilities of
307 Zhejiang University School of Medicine for the support in confocal microscopy and transmission
308 electron microscopy. We acquired many valuable fly strains from Bloomington *Drosophila* Stock
309 Center, TsingHua Fly Center and Vienna *Drosophila* Resource Center, we are grateful for their
310 efforts.

311

312 **References**

313

314 1. Halassa, M. M., Fellin, T., Takano, H., Dong, J.-H. & Haydon, P. G. Synaptic islands
315 defined by the territory of a single astrocyte. *J Neurosci* **27**, 6473–6477 (2007).
316 2. Tan, C. X. & Eroglu, C. Cell adhesion molecules regulating astrocyte–neuron interactions.
317 *Current Opinion in Neurobiology* **69**, 170–177 (2021).
318 3. Aten, S. *et al.* Ultrastructural view of astrocyte arborization, astrocyte-astrocyte and
319 astrocyte-synapse contacts, intracellular vesicle-like structures, and mitochondrial
320 network. *Prog Neurobiol* **213**, 102264 (2022).
321 4. Wenzel, J., Lammert, G., Meyer, U. & Krug, M. The influence of long-term potentiation on
322 the spatial relationship between astrocyte processes and potentiated synapses in the
323 dentate gyrus neuropil of rat brain. *Brain Research* **560**, 122–131 (1991).
324 5. Genoud, C. *et al.* Plasticity of astrocytic coverage and glutamate transporter expression
325 in adult mouse cortex. *PLoS Biol* **4**, e343 (2006).

326 6. Morel, L., Higashimori, H., Tolman, M. & Yang, Y. VGluT1+ neuronal glutamatergic
327 signaling regulates postnatal developmental maturation of cortical protoplasmic astroglia.
328 *J Neurosci* **34**, 10950–10962 (2014).
329 7. Bernardinelli, Y. *et al.* Activity-dependent structural plasticity of perisynaptic astrocytic
330 domains promotes excitatory synapse stability. *Curr Biol* **24**, 1679–1688 (2014).
331 8. Stogsdill, J. A. *et al.* Astrocytic neuroligins control astrocyte morphogenesis and
332 synaptogenesis. *Nature* **551**, 192–197 (2017).
333 9. Henneberger, C. *et al.* LTP Induction Boosts Glutamate Spillover by Driving Withdrawal
334 of Perisynaptic Astroglia. *Neuron* **108**, 919-936.e11 (2020).
335 10. Takano, T. *et al.* Chemico-genetic discovery of astrocytic control of inhibition in vivo.
336 *Nature* **588**, 296–302 (2020).
337 11. Lawal, O., Ulloa Severino, F. P. & Eroglu, C. The role of astrocyte structural plasticity in
338 regulating neural circuit function and behavior. *Glia* **70**, 1467–1483 (2022).
339 12. Xie, Y. *et al.* Astrocyte-neuron crosstalk through Hedgehog signaling mediates cortical
340 synapse development. *Cell Rep* **38**, 110416 (2022).
341 13. Nozawa, O. *et al.* Necl2/3-mediated mechanism for tripartite synapse formation.
342 *Development* **150**, dev200931 (2023).
343 14. Thomas, C. I., Ryan, M. A., McNabb, M. C., Kamasawa, N. & Scholl, B. Astrocyte
344 coverage of excitatory synapses correlates to measures of synapse structure and
345 function in ferret primary visual cortex. *Glia* **72**, 1785–1800 (2024).
346 15. Ma, Z., Stork, T., Bergles, D. E. & Freeman, M. R. Neuromodulators signal through
347 astrocytes to alter neural circuit activity and behaviour. *Nature* **539**, 428–432 (2016).
348 16. Bazargani, N. & Attwell, D. Amines, Astrocytes, and Arousal. *Neuron* **94**, 228–231 (2017).
349 17. Corkrum, M. & Araque, A. Astrocyte-neuron signaling in the mesolimbic dopamine
350 system: the hidden stars of dopamine signaling. *Neuropsychopharmacology* **46**, 1864–
351 1872 (2021).
352 18. Bariselli, S., Glangetas, C., Tzanoulinou, S. & Bellone, C. Ventral tegmental area
353 subcircuits process rewarding and aversive experiences. *J Neurochem* **139**, 1071–1080
354 (2016).
355 19. Garritsen, O., van Battum, E. Y., Grossouw, L. M. & Pasterkamp, R. J. Development,
356 wiring and function of dopamine neuron subtypes. *Nat Rev Neurosci* **24**, 134–152 (2023).
357 20. Grace, A. A. Dysregulation of the dopamine system in the pathophysiology of
358 schizophrenia and depression. *Nat Rev Neurosci* **17**, 524–532 (2016).
359 21. DiCarlo, G. E. *et al.* Autism-linked dopamine transporter mutation alters striatal dopamine
360 neurotransmission and dopamine-dependent behaviors. *J Clin Invest* **129**, 3407–3419
361 (2019).
362 22. McCutcheon, R. A., Abi-Dargham, A. & Howes, O. D. Schizophrenia, Dopamine and the
363 Striatum: From Biology to Symptoms. *Trends Neurosci* **42**, 205–220 (2019).
364 23. Benes, F. M. Emerging principles of altered neural circuitry in schizophrenia. *Brain Res*
365 *Brain Res Rev* **31**, 251–269 (2000).

24. DiCarlo, G. E. & Wallace, M. T. Modeling dopamine dysfunction in autism spectrum disorder: From invertebrates to vertebrates. *Neuroscience & Biobehavioral Reviews* **133**, 104494 (2022).
25. Corkrum, M. *et al.* Dopamine-Evoked Synaptic Regulation in the Nucleus Accumbens Requires Astrocyte Activity. *Neuron* **105**, 1036-1047.e5 (2020).
26. Petrelli, F. *et al.* Dysfunction of homeostatic control of dopamine by astrocytes in the developing prefrontal cortex leads to cognitive impairments. *Mol Psychiatry* **25**, 732–749 (2020).
27. Requie, L. M. *et al.* Astrocytes mediate long-lasting synaptic regulation of ventral tegmental area dopamine neurons. *Nat Neurosci* **25**, 1639–1650 (2022).
28. Petrelli, F. *et al.* Disruption of Astrocyte-Dependent Dopamine Control in the Developing Medial Prefrontal Cortex Leads to Excessive Grooming in Mice. *Biol Psychiatry* **93**, 966–975 (2023).
29. Lisé, M.-F. & El-Husseini, A. The neuroligin and neurexin families: from structure to function at the synapse. *Cell Mol Life Sci* **63**, 1833–1849 (2006).
30. Südhof, T. C. Synaptic Neurexin Complexes: A Molecular Code for the Logic of Neural Circuits. *Cell* **171**, 745–769 (2017).
31. Hale, W. D., Südhof, T. C. & Huganir, R. L. Engineered adhesion molecules drive synapse organization. *Proc Natl Acad Sci U S A* **120**, e2215905120 (2023).
32. Connor, S. A. & Siddiqui, T. J. Synapse organizers as molecular codes for synaptic plasticity. *Trends Neurosci* **46**, 971–985 (2023).
33. Uchigashima, M., Ohtsuka, T., Kobayashi, K. & Watanabe, M. Dopamine synapse is a neuroligin-2-mediated contact between dopaminergic presynaptic and GABAergic postsynaptic structures. *Proc Natl Acad Sci U S A* **113**, 4206–4211 (2016).
34. Cho, W. *et al.* On-Site Formation of Functional Dopaminergic Presynaptic Terminals on Neuroligin-2-Modified Gold-Coated Microspheres. *ACS Appl Mater Interfaces* **16**, 3082–3092 (2024).
35. Ducrot, C. *et al.* Conditional deletion of neurexins dysregulates neurotransmission from dopamine neurons. *Elife* **12**, e87902 (2023).
36. Bottos, A. *et al.* The synaptic proteins neurexins and neuroligins are widely expressed in the vascular system and contribute to its functions. *Proc Natl Acad Sci U S A* **106**, 20782–20787 (2009).
37. Sakers, K. & Eroglu, C. Control of neural development and function by glial neuroligins. *Curr Opin Neurobiol* **57**, 163–170 (2019).
38. Ackerman, S. D., Perez-Catalan, N. A., Freeman, M. R. & Doe, C. Q. Astrocytes close a motor circuit critical period. *Nature* **592**, 414–420 (2021).
39. Aerobic glycolysis in the primate brain: reconsidering the implications for growth and maintenance | Brain Structure and Function. https://link.springer.com/article/10.1007/s00429-013-0662-z.

405 40. Nortley, R. & Attwell, D. Control of brain energy supply by astrocytes. *Current Opinion in*
406 *Neurobiology* **47**, 80–85 (2017).
407 41. Muthukumar, A. K., Stork, T. & Freeman, M. R. Activity-dependent regulation of astrocyte
408 GAT levels during synaptogenesis. *Nat Neurosci* **17**, 1340–1350 (2014).
409 42. Volkenhoff, A. *et al.* Glial Glycolysis Is Essential for Neuronal Survival in Drosophila. *Cell*
410 *Metabolism* **22**, 437–447 (2015).
411 43. Feinberg, E. H. *et al.* GFP Reconstitution Across Synaptic Partners (GRASP) defines cell
412 contacts and synapses in living nervous systems. *Neuron* **57**, 353–363 (2008).
413 44. Gordon, M. D. & Scott, K. Motor control in a Drosophila taste circuit. *Neuron* **61**, 373–384
414 (2009).
415 45. Doherty, J., Logan, M. A., Taşdemir, O. E. & Freeman, M. R. Ensheathing glia function as
416 phagocytes in the adult Drosophila brain. *J Neurosci* **29**, 4768–4781 (2009).
417 46. Berry, J. A., Cervantes-Sandoval, I., Chakraborty, M. & Davis, R. L. Sleep Facilitates
418 Memory by Blocking Dopamine Neuron-Mediated Forgetting. *Cell* **161**, 1656–1667
419 (2015).
420 47. MacNamee, S. E. *et al.* Astrocytic glutamate transport regulates a Drosophila CNS
421 synapse that lacks astrocyte ensheathment. *Journal of Comparative Neurology* **524**,
422 1979–1998 (2016).
423 48. Fouquet, W. *et al.* Maturation of active zone assembly by Drosophila Bruchpilot. *J Cell*
424 *Biol* **186**, 129–145 (2009).
425 49. Sanghera, M. K., Trulson, M. E. & German, D. C. Electrophysiological properties of
426 mouse dopamine neurons: In vivo and in vitro studies. *Neuroscience* **12**, 793–801 (1984).
427 50. Ma, Z. & Freeman, M. R. TrpML-mediated astrocyte microdomain Ca2+ transients
428 regulate astrocyte-tracheal interactions. *Elife* **9**, e58952 (2020).
429 51. Vömel, M. & Wegener, C. Neuroarchitecture of Aminergic Systems in the Larval Ventral
430 Ganglion of Drosophila melanogaster. *PLOS ONE* **3**, e1848 (2008).
431 52. Pellerin, L. & Magistretti, P. J. Glutamate uptake into astrocytes stimulates aerobic
432 glycolysis: a mechanism coupling neuronal activity to glucose utilization. *Proc Natl Acad*
433 *Sci U S A* **91**, 10625–10629 (1994).
434 53. Almeida, A., Jimenez-Blasco, D. & Bolaños, J. P. Cross-talk between energy and redox
435 metabolism in astrocyte-neuron functional cooperation. *Essays Biochem* **67**, 17–26
436 (2023).
437 54. Bassett, A. R., Tibbit, C., Ponting, C. P. & Liu, J.-L. Highly efficient targeted mutagenesis
438 of Drosophila with the CRISPR/Cas9 system. *Cell Rep* **4**, 220–228 (2013).
439 55. Wang, H. *et al.* One-step generation of mice carrying mutations in multiple genes by
440 CRISPR/Cas-mediated genome engineering. *Cell* **153**, 910–918 (2013).
441 56. Cong, L. *et al.* Multiplex genome engineering using CRISPR/Cas systems. *Science* **339**,
442 819–823 (2013).
443 57. Ren, X. *et al.* Optimized gene editing technology for Drosophila melanogaster using germ
444 line-specific Cas9. *Proc Natl Acad Sci U S A* **110**, 19012–19017 (2013).

445 58. Rouget, M., Araud, D., Seite, R., Prochiantz, A. & Autillo-Touati, A. Astrocyte-regulated
446 synaptogenesis: an in vitro ultrastructural study. *Neurosci Lett* **150**, 85–88 (1993).
447 59. Slezak, M. & Pfrieger, F. W. New roles for astrocytes: regulation of CNS synaptogenesis.
448 *Trends Neurosci* **26**, 531–535 (2003).
449 60. Baldwin, K. T. & Eroglu, C. Molecular mechanisms of astrocyte-induced synaptogenesis.
450 *Curr Opin Neurobiol* **45**, 113–120 (2017).
451 61. Tan, C. X., Burrus Lane, C. J. & Eroglu, C. Role of astrocytes in synapse formation and
452 maturation. *Curr Top Dev Biol* **142**, 371–407 (2021).
453 62. Farizatto, K. L. G. & Baldwin, K. T. Astrocyte-synapse interactions during brain
454 development. *Curr Opin Neurobiol* **80**, 102704 (2023).
455 63. Irala, D. *et al.* Astrocyte-secreted neurocan controls inhibitory synapse formation and
456 function. *Neuron* **112**, 1657-1675.e10 (2024).
457 64. Stork, T., Sheehan, A., Tasdemir-Yilmaz, O. E. & Freeman, M. R. Neuron-glia
458 interactions through the Heartless FGF receptor signaling pathway mediate
459 morphogenesis of Drosophila astrocytes. *Neuron* **83**, 388–403 (2014).
460 65. Chen, J. *et al.* Astrocyte growth is driven by the Tre1/S1pr1 phospholipid-binding G
461 protein-coupled receptor. *Neuron* **112**, 93-112.e10 (2024).
462 66. Lee, T. & Luo, L. Mosaic analysis with a repressible cell marker (MARCM) for *Drosophila*
463 neural development. *Trends in Neurosciences* **24**, 251–254 (2001).
464 67. Chen, Y. *et al.* Cell-type-specific labeling of synapses in vivo through synaptic tagging
465 with recombination. *Neuron* **81**, 280–293 (2014).
466 68. Harzer, H., Berger, C., Conder, R., Schmauss, G. & Knoblich, J. A. FACS purification of
467 Drosophila larval neuroblasts for next-generation sequencing. *Nat Protoc* **8**, 1088–1099
468 (2013).
469 69. Talay, M. *et al.* Transsynaptic Mapping of Second-Order Taste Neurons in Flies by trans-
470 Tango. *Neuron* **96**, 783-795.e4 (2017).
471 70. Corrales, M. *et al.* A single-cell transcriptomic atlas of complete insect nervous systems
472 across multiple life stages. *Neural Dev* **17**, 8 (2022).
473 71. Dillon, N. *et al.* Single cell RNA-seq analysis reveals temporally-regulated and
474 quiescence-regulated gene expression in Drosophila larval neuroblasts. *Neural Dev* **17**, 7
475 (2022).
476 72. Corrales, M. *et al.* A single-cell transcriptomic atlas of complete insect nervous systems
477 across multiple life stages. *Neural Dev* **17**, 8 (2022).
478 73. Pliner, H. A., Shendure, J. & Trapnell, C. Supervised classification enables rapid
479 annotation of cell atlases. *Nat Methods* **16**, 983–986 (2019).
480 74. Hoang, B. & Chiba, A. Single-Cell Analysis of *Drosophila* Larval Neuromuscular
481 Synapses. *Developmental Biology* **229**, 55–70 (2001).
482 75. Pérez-Moreno, J. J. & O'Kane, C. J. GAL4 Drivers Specific for Type Ib and Type Is Motor
483 Neurons in Drosophila. *G3 (Bethesda)* **9**, 453–462 (2019).

484 76. Cooper, R. L. & Neckameyer, W. S. Dopaminergic modulation of motor neuron activity
485 and neuromuscular function in Drosophila melanogaster. *Comp Biochem Physiol B*
486 *Biochem Mol Biol* **122**, 199–210 (1999).
487 77. Dasari, S. & Cooper, R. L. Modulation of sensory-CNS-motor circuits by serotonin,
488 octopamine, and dopamine in semi-intact Drosophila larva. *Neurosci Res* **48**, 221–227
489 (2004).
490 78. Dodson, P. D. *et al.* Representation of spontaneous movement by dopaminergic neurons
491 is cell-type selective and disrupted in parkinsonism. *Proc Natl Acad Sci U S A* **113**,
492 E2180-2188 (2016).
493 79. Engelhard, B. *et al.* Specialized coding of sensory, motor and cognitive variables in VTA
494 dopamine neurons. *Nature* **570**, 509–513 (2019).
495 80. Marquis, M. & Wilson, R. I. Locomotor and olfactory responses in dopamine neurons of
496 the Drosophila superior-lateral brain. *Curr Biol* **32**, 5406-5414.e5 (2022).
497 81. Risse, B. *et al.* FIM, a novel FTIR-based imaging method for high throughput locomotion
498 analysis. *PLoS One* **8**, e53963 (2013).
499 82. Risse, B., Otto, N., Berh, D., Jiang, X. & Klämbt, C. FIM imaging and FIMtrack: two new
500 tools allowing high-throughput and cost effective locomotion analysis. *J Vis Exp* 52207
501 (2014) doi:10.3791/52207.
502 83. Lahiri, S. *et al.* Two alternating motor programs drive navigation in Drosophila larva.
503 *PLoS One* **6**, e23180 (2011).
504 84. Zarin, A. A., Mark, B., Cardona, A., Litwin-Kumar, A. & Doe, C. Q. A multilayer circuit
505 architecture for the generation of distinct locomotor behaviors in Drosophila. *Elife* **8**,
506 e51781 (2019).
507 85. Loveless, J., Lagogiannis, K. & Webb, B. Modelling the mechanics of exploration in larval
508 Drosophila. *PLoS Comput Biol* **15**, e1006635 (2019).
509 86. Bogaciu, C. A. & Rizzoli, S. O. Membrane trafficking of synaptic adhesion molecules. *J*
510 *Physiol* (2024) doi:10.1113/JP286401.
511 87. Hoffman, R. C. *et al.* Structural characterization of recombinant soluble rat neuroligin 1:
512 mapping of secondary structure and glycosylation by mass spectrometry. *Biochemistry*
513 **43**, 1496–1506 (2004).
514 88. Comoletti, D., Trobiani, L., Chatonnet, A., Bourne, Y. & Marchot, P. Comparative
515 mapping of selected structural determinants on the extracellular domains of
516 cholinesterase-like cell-adhesion molecules. *Neuropharmacology* **184**, 108381 (2021).
517 89. De Jaco, A. *et al.* Neuroligin trafficking deficiencies arising from mutations in the
518 alpha/beta-hydrolase fold protein family. *J Biol Chem* **285**, 28674–28682 (2010).
519 90. Jeong, J., Paskus, J. D. & Roche, K. W. Posttranslational modifications of neuroligins
520 regulate neuronal and glial signaling. *Curr Opin Neurobiol* **45**, 130–138 (2017).
521 91. Bemben, M. A., Shipman, S. L., Nicoll, R. A. & Roche, K. W. The cellular and molecular
522 landscape of neuroligins. *Trends Neurosci* **38**, 496–505 (2015).

523 92. Cast, T. P. *et al.* An Autism-Associated Mutation Impairs Neuroligin-4 Glycosylation and
524 Enhances Excitatory Synaptic Transmission in Human Neurons. *J Neurosci* **41**, 392–407
525 (2021).
526 93. Benner, O. *et al.* Multiple N-linked glycosylation sites critically modulate the synaptic
527 abundance of neuroligin isoforms. *J Biol Chem* **299**, 105361 (2023).
528 94. Leno, G. H. & Ledford, B. E. ADP-ribosylation of the 78-kDa glucose-regulated protein
529 during nutritional stress. *Eur J Biochem* **186**, 205–211 (1989).
530 95. Maher, F. & Harrison, L. C. Stimulation of glucose transporter (GLUT1) mRNA and
531 protein expression by inhibitors of glycosylation. *Biochim Biophys Acta* **1089**, 27–32
532 (1991).
533 96. Tomás, M. *et al.* Ethanol impairs monosaccharide uptake and glycosylation in cultured rat
534 astrocytes. *J Neurochem* **83**, 601–612 (2002).
535 97. Xi, H., Kurtoglu, M. & Lampidis, T. J. The wonders of 2-deoxy-D-glucose. *IUBMB Life* **66**,
536 110–121 (2014).
537 98. Rudman, N., Gornik, O. & Lauc, G. Altered N-glycosylation profiles as potential
538 biomarkers and drug targets in diabetes. *FEBS Lett* **593**, 1598–1615 (2019).
539 99. Hawkinson, T. R. *et al.* In situ spatial glycomic imaging of mouse and human Alzheimer's
540 disease brains. *Alzheimers Dement* **18**, 1721–1735 (2022).
541 100. Tio, M., Toh, J., Fang, W., Blanco, J. & Udolph, G. Asymmetric cell division and Notch
542 signaling specify dopaminergic neurons in Drosophila. *PLoS One* **6**, e26879 (2011).
543 101. Bonvento, G. & Bolaños, J. P. Astrocyte-neuron metabolic cooperation shapes brain
544 activity. *Cell Metab* **33**, 1546–1564 (2021).

545
546

547 **Figures**

548

549 **Figure 1. Perisynaptic astrocyte ensheathment of DAergic synapses.**

550

551 (A) Third instar larval CNS with the VNC highlighted (scale bar: 50 μm). Reconstituted GFP
552 (reconst. GFP) reveals astrocyte contact sites (arrowheads and open arrowheads) with DAergic
553 neuronal processes labeled by myristoylated tdTomato (mtdTomato) (scale bars: 5 μm). Open
554 arrowheads identify typical PEAPODs that resemble synaptic boutons on terminal branches of
555 DAergic neurons. Brp: Bruchpilot (presynaptic marker).

556 (B) Single-cell PEAPODs and synaptic labeling of the DAergic neuron in larval ventral nerve
557 cord (n = 11) (scale bars: 10 μm).

558 (C) Inset zoom in (B), arrowheads denote PEAPODs^{+} Brp.S-mStraw puncta (scale bar: 2 μm).

559 (D) Schematic drawing of the PEAPODs. Note that GFP reconstitutes at the contact site
560 between the astrocyte sheath and DAergic synapse.

561 (E–H) PEAPODs intensity vs. spontaneous DAergic neuronal burst activation (Ca^{2+}, mR-
562 GECO1) (n = 12). RP, SP, and DP: rising, sustaining, and decay periods, respectively. The
563 area under the curve (AUC) was calculated to show the accumulative PEAPODs response over
564 time. max.: Maximum.

565 (I) PEAPODs intensity. Genetically manipulated DAergic neuronal activity (arrows, up or down)
566 as indicated (n = 8–12). *th*: DAergic neuron driver. *mKcnj2*, *TNT-G* inactive controls: *mKcnj2.nc*,
567 *TNT-Q*.

568 (F), (G), (H), one-way ANOVA with Tukey's test. (I), unpaired t-test. $^{**}P < 0.01$. ns: Not
569 significant, FC: Fold change.

570

571 **Figure 2. Astrocyte glycolysis deficiency increases PEAPODs abundance.**

572

573 (A) Biochemical pathway of glycolysis. Dotted arrows indicate the intermediate steps not shown.
574 The double-headed arrow denotes reversible reactions.

575 (B–E) PEAPODs and abundance analysis (scale bars: 50 μm). Gene knockdown (KD) in the
576 astrocyte (astro) using RNAi were driven by the *alrm* driver. Genotypes as indicated (n = 10–
577 12. In E, 784–2583 individual PEAPODs in total).

578 (F) Pyk (α-Pyk) was enriched in astrocytes (scale bars: 50 μm).

579 (G) *pyk* KD diminished Pyk expression (scale bars: 10 μm). In (F) and (G), mCD8-GFP labeled
580 astrocytes, and α-Repo stained glial cell nuclei.

581 (H–K) PEAPODs and abundance analysis (scale bars: 25 μm). Genotypes as indicated (n = 10.
582 In K, 88–180 individual PEAPODs in total).

583 (C), (D), one-way ANOVA with Tukey's test. (I), (J), unpaired t-test. (E), (K), Kolmogorov-
584 Smirnov test. *P < 0.05, **P < 0.01, ***P < 0.001, ****P < 0.0001. ns: Not significant, FC: Fold
585 change.

586

587 **Figure 3. Glycolysis-deficient astrocytes promote DAergic synaptogenesis.**

588

589 (A) Astrocyte number. Genotypes as indicated (n = 12).

590 (B) Normal neuropile (marked by α-Brp) infiltration by the astrocyte in the *pyk*$^{11/7}$ mutant (scale
591 bars: 20 μm). xz confocal sections show the infiltration in the dorsal (d)-ventral (v) axis of the
592 VNC. Genotypes as indicated (n = 12). *alrm*: Astrocyte driver, mCD8-GFP: Membrane-tethered
593 GFP, Brp: Bruchpilot (presynaptic marker).

594 (C) Mean Brp levels. Genotypes as indicated (n = 12).

595 (D and E) Single astrocyte MARCM clone. Genotypes as indicated (n = 20–26). MARCM:
596 mosaic analysis with a repressible cell marker.

597 (F and G) Endogenous Brp (Brp-GFP) in DAergic neurons (scale bars: 25 μm; 5 μm in the inset
598 zoom). Genotypes as indicated (n = 12). astro: Astrocyte, KD: Knockdown.

599 (H and I) Sections by transmission electron microscopy (scale bars: 500 nm). Color shade:
600 synapses, blue; astrocyte processes, orange. Note that perisynaptic astrocyte process
601 (arrowheads) were more often observed in astro *pyk* KD. Genotypes as indicated (n = 311–313
602 frames from 5 larval CNS). Frame size, 4.28 μm (width) × 4.41 μm (length). astro: Astrocyte,
603 KD: Knockdown.

604 Unpaired t-test. **P < 0.01. ns: Not significant, FC: Fold change.

605

606 **Figure 4. Astrocyte glycolysis deficiency causes biased DAergic wiring.**

607

608 (A) Schematic protocol for profiling postsynaptic partners (labeled by *trans*-Tango) wired to
609 DAergic neurons. FACS: Fluorescence-activated cell sorting, *th*: DAergic neuron driver, *trans*-
610 Tango: Transsynaptic labeling system.

611 (B) Clustering of *nsyb*$^{+}$, *para*$^{+}$ mature neurons (ctrl, n = 5589; astrocyte [astro] *pyk* knockdown
612 [KD], n = 7236). Note that cluster 12 is distant to the others. uMAP: Uniform manifold
613 approximation and projection.

614 (C) Annotated MNs (ctrl, n = 50; astro *pyk* KD, n = 131) in the UMAP. MNs gathered in cluster
615 12.

616 (D) Close-up view of cluster 12 MNs.

617 (E) Plotting FCs in the cell number of annotated populations, astro *pyk* KD vs. ctrl. The MN
618 showed the highest FC and followed the neuropeptidergic (NP) neuron and the DAergic neuron.
619 glu: Glutamatergic, GABA: GABAergic, cho: Cholinergic, ser: Serotoninergic, OA/TA: Octop-
620 /tyr-aminergic, FC: Fold change.

621

622 **Figure 5. Biased DAergic wiring alters locomotion patterns.**

623

624 (A) Schematic illustration of *Drosophila* larval locomotive movements. Reorientation attempts
625 intervene between peristaltic sessions.

626 (B) Recorded larval locomotion trajectories (scale bars: 2 cm). Astrocyte *pyk* RNAi larvae
627 travelled in paths with dense branches; six larvae per recording. Genotypes as indicated (n =
628 30). *alrm*: Astrocyte driver.

629 (C–H) Quantitative analysis of larval locomotion. Genotypes as indicated (n = 30). Pausing rate
630 (C): The number of frames the larva pauses/the total number of frames the larva appears ×
631 100%, sweeping rate (D): The number of frames the larva sweeps/the total number of frames
632 the larva appears × 100%, bending strength (E): Median bending angle, max. velocity (F):
633 Maximum velocity, peristalsis efficiency (G): Distance per peristalsis, peristalsis frequency (H):
634 Peristalses per second). One-way ANOVA with Tukey's test. $^{**}P < 0.01$, $^{****}P < 0.0001$. ns:
635 Not significant, FC: Fold change.

636

637 **Figure 6. Astrocyte glycolysis deficiency disables astrocyte-DAergic neuronal Nlg2-Nrx1**
638 **signaling.**

639

640 (A–H) PEAPODs and abundance analysis (scale bars: 50 μm). Genotypes as indicated (n =
641 10–12; in D, 659–2286; in H, 1756–3975 individual PEAPODs in total). *alrm*: Astrocyte driver,
642 *th*: DAergic neuron driver, KD: Knockdown.

643 (I and J) Endogenous Brp (Brp-GFP) in DAergic neurons (scale bars: 25 μm; 5 μm in the inset
644 zoom). Genotypes as indicated (n = 12). Brp: Bruchpilot (presynaptic marker).

645 (K and L) Glycolysis deficiency led to intra-astrocyte Nlg2 bodies (arrowheads) (scale bars: 5
646 μm; 2 μm in the inset zoom). The dotted line marks the astrocyte soma. Genotypes as indicated
647 (n = 12). mCD8-GFP: Membrane-tethered GFP.

648 (M) The ER reporter GFP-KDEL decorated Nlg2 bodies (arrowheads) (scale bars: 2 μm).

649 (B), (C), (F), (G), (J), (L), unpaired t-test. (D), (H), Kolmogorov-Smirnov test. ***$P < 0.001$, ****P
650 < 0.0001. ns: Not significant, FC: Fold change.

Supporting Information (SI) for

Metabolic basis of the astrocyte-synapse interaction governs dopaminergic-motor connection

Yanru Xu[#], Piaoping Kong[#], Mengqi Wang, Yanyun Mao, Zhiguo Ma[*]

[#]These authors contributed equally

[*]Corresponding to: zgma@zju.edu.cn

Email: zgma@zju.edu.cn

Materials and Methods

Drosophila husbandry and stocks

Flies were cultured in cornmeal food at 25°C, unless stated otherwise. Detailed stock information is provided in Table S4.

Molecular biology and transgenic flies

The construct *lexAop2-pyk^{RNAi}* was assembled in alignment with attP/attB site-directed transgene integration in *Drosophila*, as illustrated in Fig. S3D. The *lexAop2-pyk^{RNAi}* transgenic fly was obtained via standard germline microinjection.

Single-cell clone induction

The genotype of larvae for single-neuron PEAPODs and synaptic labeling: *alrm-LexA, lexAop-CD4-spGFP^{11}/UAS-brp.S-mStraw*; *hs-FLPG5, tub>Gal80>/th-Gal4, UAS-CD4-spGFP$^{1-10}$*. Eleven single VNC DAergic neurons (out of 120 3rd instar larval CNSs dissected) were obtained by 37°C heatshock for 10 min at 22 h after egg laying. Confocal images were taken using a Zeiss LSM 900 with Airyscan (objective lens, Plan-Apochromat 63×/1.40 NA, Oil, DIC M27). To quantitate astrocyte-DAergic synapse association: Image J plugin 3D objects counter was used to create two new image stacks by segmenting Brp.S-mStraw puncta and PEAPODs in confocal images from separate channels. The two image stacks (Brp.S-mStraw objects [BO], PEAPODs objects [PO]) were merged, and the association between BO and PO was examined.

Genotypes for generating clones by mosaic analysis with a repressible cell marker (MARCM): control, *alrm-Gal4, UAS-mCD8-GFP/repo-FLP; FRT82B/FRT82B, tub-Gal80*; *pyk* mutant, *alrm-Gal4, UAS-mCD8-GFP/repo-FLP; FRT82B, pyk^{7}/FRT82B, tub-Gal80*. We took confocal images with an inverted Olympus IXplore SpinSR spinning disk confocal super resolution microscope (objective lens, UPLXAPO 60×/1.5 NA, Oil) and measured astrocyte volume in Imaris software.

Live imaging and data analysis

We followed the live imaging protocol described by Ma et al. with minor modifications[1]. The 3rd instar larval CNS was dissected in low Ca^{2+} (0.3 mM) live imaging buffer (110 mM NaCl, 5.4 mM KCl, 1.2 mM $CaCl_2$, 0.8 mM $MgCl_2$, 10 mM D-glucose, 10 mM HEPES, pH 7.2). Next, the CNS was immediately transferred into a cell culture dish (Ø 28.2 mm; glass bottom, Ø 20 mm) filled with standard Ca^{2+} (1.2 mM) live imaging buffer. Time-series movies were taken with an inverted Olympus IXplore SpinSR spinning disk confocal super resolution microscope

(objective lens, UPLXAPO 40×/0.95 NA, Air) by alternating 488 nm and 561 nm laser channels. The movies were corrected for drifts by Fast4Dreg, and the fluorescence intensities of PEAPODs and mR-GECO1 were quantitated over time by TrackMate in Image J. The dF/F was calculated, and data points were plotted in GraphPad Prism.

PEAPODs imaging and abundance analysis

The larval CNS was dissected and fixed as described below. After washing off the fixative, samples were incubated in mounting medium (90% glycerol + 10% 1× phosphate buffered saline [PBS]) overnight. Confocal images were taken using an Olympus FV3000 (objective lens, UPLAPO 60×/1.50 NA, Oil). The field of view (FOV) runs 212.1 μm × 212.1 μm, which can accommodate all abdominal segments of the 3rd instar larval VNC. The PEAPODs intensity was determined by measuring the mean intensity of the reconstituted GFP (confocal z-stack projections by maximum intensity) in Image J. The Image J plugin 3D objects counter was used for 3D segmentation, numbering, and volume sizing of PEAPODs. PEAPODs from abdominal segments a1–a2 (cropping, 62.2 μm × 165.3 μm, width × length) are shown in Figs. 2B, 2H, 6A, 6E, and S2A–S2D.

Thermogenetic activation of DAergic neurons

Control and *th>TrpA1* larvae were cultured in an incubator at 18°C before thermogenetic activation in a 29°C water bath. The larval cohort of each treatment (10-min, 20-min and 30-min) was kept in the water bath until the dissection was completed within the next 10 min.

Binary expression systems for gene knockdown in astrocytes

We used LexA/lexAop to knock down *pyk* in Figs. 3F, 3G, 4, S3E–S3G, S4D, S4E and S5, while Gal4/UAS was used in the others.

***pyk* mutagenesis by CRISPR-Cas9**

Flies carrying $pyk^{TKO.GS03070}$ (for the expression of short guide RNA targeting *pyk*) and *nos-Cas9* (for germline Cas9 expression) were crossed to obtain the F1 progeny. Next, F1 males were crossed to a balancer strain, and individual F3 stocks were created by mating single F2 flies to the same balancer strain. Two frameshift deletions of *pyk* (i.e., alleles pyk^{11} and pyk^{7}) were recovered in F3 stocks.

Antibodies, immunohistochemistry, western blotting, and transmission electron microscopy

The following primary antibodies were used in this study: α-Brp (1:100, nc82, DSHB), α-Repo (1:100, 8D12, DSHB), Alexa Fluor 647 AffiniPure goat anti-HRP (1:200, 123-605-021, Jackson Immunoresearch), α-tubulin (1:5000, ab52866, Abcam), α-Pyk (1:200–1:1000), and α-Nlg2 (1:200). Polyclonal α-Pyk, α-Nlg2 antibodies were produced by immunizing rabbits with synthetic peptides (Pyk, 199 a.a.–212 a.a., EVENGGSLGSRKGV; Nlg2, 295 a.a.–308 a.a., RQRRNTDDTTGEPK) conjugated to keyhole limpet hemocyanin (KLH).

The following secondary antibodies were used in this study: AffiniPure goat anti-mouse Alexa Fluor 647 (1:200, 115-605-062), AffiniPure goat anti-rabbit Alexa Fluor 594 (1:1000, 111-585-045), and peroxidase AffiniPure goat anti-rabbit (1:5000, 111-035-003) (Jackson Immunoresearch).

Immunohistochemistry: Briefly, larval CNSs were dissected in 1× PBS and fixed in 4% PFA for 20 min. After washing off the PFA in 1× PBS, the samples were incubated in 0.3% PBST (1× PBS + 0.3% Triton) for 2 h. Next, the samples were incubated in primary antibody diluted in 0.1% PBST for 72 h at 4°C. The primary antibody was pipetted out, and the samples were washed three times in 0.1% PBST for 10 min each time. The samples were then incubated in secondary antibody diluted in 0.1% PBST for 4 h at room temperature. After removing the secondary antibody, the samples underwent three 10-min washes in 0.1% PBST and one 5-min wash in 1× PBS. Finally, the samples were mounted in Vectashield mounting medium for confocal imaging.

Western blotting: The 2nd instar larval CNS was dissected and homogenized in RIPA (89900, Thermo Fisher) supplemented with proteinase inhibitor cocktail. The lysates were centrifuged (12,000 rpm) at 4°C for 15 min. The supernatants were collected and the total protein concentrations were quantitated using BCA assays. Heat-denatured samples (1 μg/μl) were resolved using 4%–12% gradient SDS-PAGE gels. We followed the standard western blotting procedure for gel-to-membrane (PVDF) protein transfer, membrane blocking, primary antibody incubation (α-Pyk, 1:1000; 4°C, overnight), and secondary antibody binding (peroxidase AffiniPure goat anti-rabbit; 1:5000, room temperature, 1 h) with necessary washing in 1× PBS + 0.1% Tween-20 during each stepwise transition. ECL (34580, Thermo Fisher) was applied on the membrane, and chemiluminescent signals were recorded using a gel imager. Stripping was performed to remove the antibodies from the membrane. The above steps, starting from the primary antibody incubation, were repeated to detect the loading control using α-tubulin.

Transmission electron microscopy: The 3rd instar larval CNS was dissected in 0.1 M PBS and immediately fixed overnight in 2.5% glutaraldehyde (diluted in 0.1 M PBS) at 4 °C. The samples were then rinsed in 0.1 M PBS (three times, 10 min each time) and post-fixed with 2% uranyl acetate for 30 min at room temperature. After a 5-min washing in dH_2O, the samples were gradually dehydrated in 50%, 70%, 90% (one time,15 min each time) and 100% (twice,

20 min each time) ethanol. The samples were then incubated in 100% acetone (twice, 20 min each time), infiltrated in 50%/50% Epon 812 resin/acetone mixture for 2 h and in 75%/25% Epon 812 resin/acetone mixture overnight. On next day, the samples were carefully orientated in 100% Epon 812 resin in plastic embedding molds and left at 65 °C for polymerization. Ventral nerve cords of the samples were ultrathin sectioned. The sections were placed on copper grids, contrasted in 4% uranyl acetate for 30 min and inspected with a Thermo Scientific Talos L120C TEM at 120 kV.

FACS, scRNA-seq, data analysis, and cell type annotation

Fifty 3rd instar larval CNSs per genotype were dissected in ice-cold Rinaldini's solution. The sample collection, cell dissociation, and cell sorting for harvesting mtdTomato$^+$ cells by FACS were performed as described by Harzer et al.[2]. The 10× Genomics scRNA-seq was conducted following the manufacturer's guidelines. Briefly, the 10× library was constructed by amplifying 10× barcoded cDNA obtained by poly (T) RT-PCR from single-cell gel bead-in emulsions (GEMs). For quality control, the insert sizes and the concentration of the 10× library were validated using electrophoresis (Agilent 2100 Bioanalyzer) and qPCR (StepOnePlus Real-Time PCR System), respectively. The 10× library was sequenced on an Illumina HiSeq PE150 sequencer. The RNA sequencing reads were aligned to the released reference *Drosophila_melanogaster*/dmel_r6.54. Data analysis and visualization were performed using Cell Ranger and Seurat. We annotated cell types using customized marker genes from the literature and Garnett software[3–5].

Larval tracking and locomotion analysis

The larval locomotion was recorded using frustrated total internal reflection (FTIR)-based imaging (FIM) method at 10 fps for 90 s. For each indicated genotype, 30 larvae were recorded (six larvae per recording × five recordings). The locomotion was analyzed to calculate the sweeping rate, pausing rate, and maximum speed using the FIMTrack built-in tools[6,7]. The bending strength (i.e., median bending angle), peristalsis efficiency (i.e., distance per peristalsis), and peristalsis frequency (i.e., peristalses per second) were quantitated by pyFIM (Python package for analysis of FIMTrack data, https://github.com/schlegelp/pyfim). The minimum track length in frames was set to 50. Data filtering owing to larval collision, larval disappearance, and return in FOV may result in slightly more or less than 30 data points per genotype depending on the analysis performed. The sweeping rate was calculated as follows: the number of frames the larva sweeps/the total number of frames the larva appears × 100%. The pausing rate was calculated as follows: the number of frames the larva pauses/the total number of frames the larva appears × 100%.

Statistical analysis

Sample sizes were chosen to meet published standards. All experiments were technically repeated at least twice (see figure legends for exact number) with similar results. Regarding single-cell RNA sequencing, dataset integration was performed to correct for technical differences between the control and astrocyte *pyk* knockdown. All data were presented as the mean ± SEM. The *P*-value was obtained by performing one-way ANOVA analysis with Tukey's test, unpaired t-test, or Kolmogorov-Smirnov test in GraphPad Prism, as indicated in the figures and figure legends.

Table S1. The summary list of cells identified by sc-RNA seq and cell type annotation

	ctrl (n)	astro *pyk* KD (n)
single cells sequenced	11815	13327
nsyb^{+}*para*$^{+}$ mature neuron	5589	7236
annotated mature neuron	3824	4793
motor neuron	50	131
glutamatergic neuron	527	629
GABAergic neuron	1205	1486
cholinergic neuron	1268	1424
serotoninergic neuron	55	79
DAergic neuron	142	174
octop-/tyr-aminergic neuron	34	43
neuropeptidergic neuron	543	827

astro: Astrocyte, KD: Knockdown, n: Cell number.

Table S2. Motor neuron subclasses connected to *Drosophila* larval DAergic system

	ctrl (n)	astro *pyk* KD (n)
type I, *vglut*$^{+}$*twit*$^{+}$	20	77
type II, *tβh*$^{+}$*twit*$^{+}$	8	25
type III, *phm*$^{+}$*twit*$^{+}$	12	28

astro: Astrocyte, KD: Knockdown, n: Cell number.

Table S3. The DNA sequence assembled for creating *lexAop2-pyk*^{RNAi} construct

13× lexAop2 *hsp70* promotor *dsRNA-GL00099* spacer *ftz* intron	AAGCTTGCATGCCTGCAGGTTACTGTACATCCATACAGTAAGTACTGTACAT CCATACAGTAAGTACTGTACATCCATACAGTAAGTACTGTACATCCATACAG TAAGTACTGTACATCCATACAGTAAGCGGAGACTCTAGCCCTAGGGCATGC CTGCAGGTTACTGTACATCCATACAGTAAGTACTGTACATCCATACAGTAAG TACTGTACATCCATACAGTAAGCGGAGACTCTAGCGCTAGCGCATGCCTGC AGGTTACTGTACATCCATACAGTAAGTACTGTACATCCATACAGTAAGTACT GTACATCCATACAGTAAGTACTGTACATCCATACAGTAAGTACTGTACATCC ATACAGTAAGCGGAGACTCTAGCACTAGTGACGTCGAGCGCCGGAGTATAA ATAGAGGCGCTTCGTCTACGGAGCGACAATTCAATTCAAACAAGCAAAGTG AACACGTCGCTAAGCGAAAGCTAAGCAAATAAACAAGCGCAGCTGAACAAG CTAAACAATCTGCAGTAAAGTGCAAGTTAAAGTGAATCAATTAAAAGTAACC AGCAACCAAGTAAATCAACTGCAACTACTGAAATCTGCCAAGAAGTAATTAT TGAATACAAGAAGAGAACTCTGCAAGTTTGTACAAAAAAGCAGGCTGCTAG CAGTCGCGTTGATTACTGTTAATAATAGTTATATTCAAGCATATTATTAACAG TAATCAACGCGGCGAATTCAGGCGAGACATCGGAGTTGAAACTAAAACTGA ATTACTAGAGTGGACATATGCACCTAGGACTAGAGCAAACTAGTTCTGATCT GCTAGACAATTGTTGGCATCAGGTAGGCATCACACACGATTAACAACCCCT AAAAATACACTTTGAAAATATTGAAAATATGTTTTTGTATACATTTTTGATATT TTCAAACAATACGCAGTTATAAAACTCATTAGCTAACCCATTTTTTCTTTGCT TATGCTTACAG

Table S4. Stock list

Name	Stock Number	Stock Center/Reference
UAS-pfk$^{RNAi\#1}$	34336	BDSC
UAS-pfk$^{RNAi\#2}$	TH201500692.S	THFC
UAS-eno$^{RNAi\#1}$	26300	BDSC
UAS-eno$^{RNAi\#2}$	TH02508.N	THFC
UAS-pyk$^{RNAi\#1}$	35218	BDSC
UAS-pyk$^{RNAi\#2}$	TH03685.N	THFC
lexAop2-pyk^{RNAi}	N/A	this study
UAS-nlg2^{RNAi}	28331	BDSC
UAS-nrx1^{RNAi}	27502	BDSC
UAS-brp$^{RNAi\#1}$	80449	BDSC
UAS-brp$^{RNAi\#2}$	25891	BDSC
w^{1118}	5905	BDSC
10× UAS-IVS-mtdTomato	32222	BDSC
th-Gal4	8848	BDSC
th-LexA	99051	BDSC
UAS-TrpA1	26263	BDSC
pyk$^{TKO.GS03070}$	78770	BDSC
nos-Cas9	TH00788.N	THFC
Brp-FSF-GFP	55753	BDSC
trans-Tango QUAS-mtdTomato-3× HA	90924	BDSC
hs-FLPG5	58356	BDSC
20× UAS-FLPG5	55806	BDSC
UAS-GFP-KDEL	9898	BDSC
UAS-mKcnj2	600376	BDSC
UAS-mKcnj2.nc	600377	BDSC
UAS-TNT-G	28838	BDSC

UAS-TNT-Q	28839	BDSC
tub>Gal80>	38881	BDSC
UAS-CD4-spGFP$^{1-10}$	93017	BDSC
lexAop-CD4-spGFP^{11}	93018	BDSC
alrm-LexA		Ma et al.[1]
alrm-Gal4		Doherty et al.[8]
UAS-brp.S-mStraw		Fouquet et al.[9]
UAS-mR-GECO1		Ma et al.[10]
repo-FLP		Stork et al.[11]
UAS-mCD8-GFP		Lee & Luo[12]

BDSC: Bloomington *Drosophila* Stock Center, THFC: TsingHua Fly Center.

Movie S1 (separate file). Z-axis confocal sections showing DAergic neuronal branches (red), PEAPODs (green) and the presynaptic marker Brp (magenta)

Movie S2 (separate file). Dual-color live imaging of spontaneous DAergic neuronal activation (shown by mR-GECO1) and PEAPODs

SI References

1. Ma, Z., Stork, T., Bergles, D. E. & Freeman, M. R. Neuromodulators signal through astrocytes to alter neural circuit activity and behaviour. *Nature* **539**, 428–432 (2016).
2. Harzer, H., Berger, C., Conder, R., Schmauss, G. & Knoblich, J. A. FACS purification of Drosophila larval neuroblasts for next-generation sequencing. *Nat Protoc* **8**, 1088–1099 (2013).
3. Pliner, H. A., Shendure, J. & Trapnell, C. Supervised classification enables rapid annotation of cell atlases. *Nat Methods* **16**, 983–986 (2019).
4. Dillon, N. *et al.* Single cell RNA-seq analysis reveals temporally-regulated and quiescence-regulated gene expression in Drosophila larval neuroblasts. *Neural Dev* **17**, 7 (2022).
5. Corrales, M. *et al.* A single-cell transcriptomic atlas of complete insect nervous systems across multiple life stages. *Neural Dev* **17**, 8 (2022).
6. Risse, B. *et al.* FIM, a novel FTIR-based imaging method for high throughput locomotion analysis. *PLoS One* **8**, e53963 (2013).
7. Risse, B., Otto, N., Berh, D., Jiang, X. & Klämbt, C. FIM imaging and FIMtrack: two new tools allowing high-throughput and cost effective locomotion analysis. *J Vis Exp* 52207 (2014) doi:10.3791/52207.
8. Doherty, J., Logan, M. A., Taşdemir, O. E. & Freeman, M. R. Ensheathing glia function as phagocytes in the adult Drosophila brain. *J Neurosci* **29**, 4768–4781 (2009).
9. Fouquet, W. *et al.* Maturation of active zone assembly by Drosophila Bruchpilot. *J Cell Biol* **186**, 129–145 (2009).
10. Ma, Z. & Freeman, M. R. TrpML-mediated astrocyte microdomain Ca2+ transients regulate astrocyte-tracheal interactions. *Elife* **9**, e58952 (2020).

11. Stork, T., Sheehan, A., Tasdemir-Yilmaz, O. E. & Freeman, M. R. Neuron-glia interactions through the Heartless FGF receptor signaling pathway mediate morphogenesis of Drosophila astrocytes. *Neuron* **83**, 388–403 (2014).
12. Lee, T. & Luo, L. Mosaic analysis with a repressible cell marker (MARCM) for *Drosophila* neural development. *Trends in Neurosciences* **24**, 251–254 (2001).

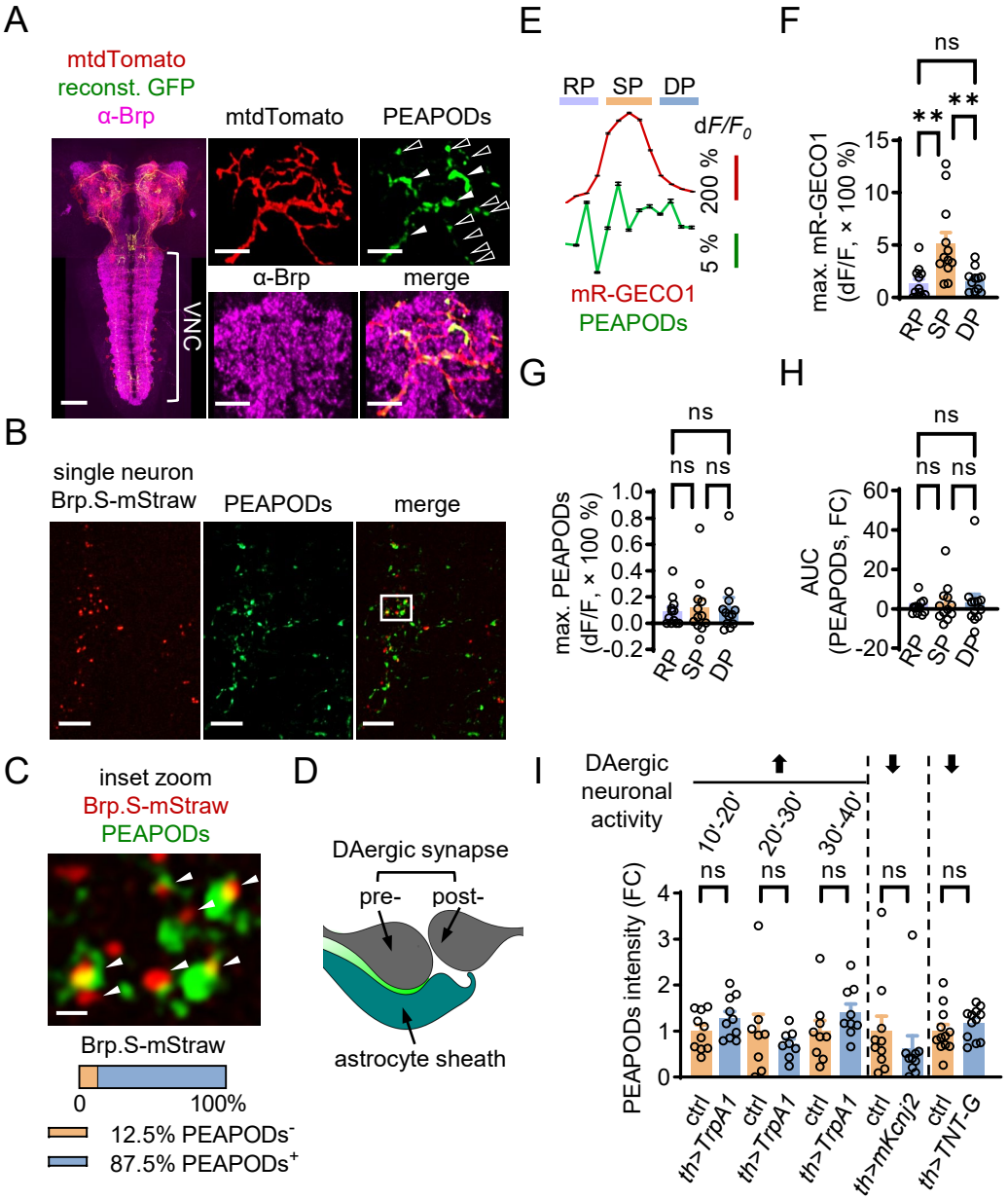
A
mtdTomato
reconst. GFP
α-Brp
mtdTomato
PEAPODs
α-Brp
merge
VNC
B
single neuron
Brp.S-mStraw
PEAPODs
merge
C
inset zoom
Brp.S-mStraw
PEAPODs
Brp.S-mStraw
0
100%
12.5% PEAPODs-
87.5% PEAPODs+
D
DAergic synapse
pre-
post-
astrocyte sheath
E
RP SP DP
dF/F0
200 %
5 %
mR-GECO1
PEAPODs
F
ns
**
**
max. mR-GECO1
(dF/F, × 100 %)
RP SP DP
G
ns
ns ns
max. PEAPODs
(dF/F, × 100 %)
RP SP DP
H
ns
ns ns
AUC
(PEAPODs, FC)
RP SP DP
I
DAergic
neuronal
activity
10'-20'
20'-30'
30'-40'
ns
PEAPODs intensity (FC)
ctrl
th>TrpA1
th>mKcnj2
th>TNT-G

Fig. 1

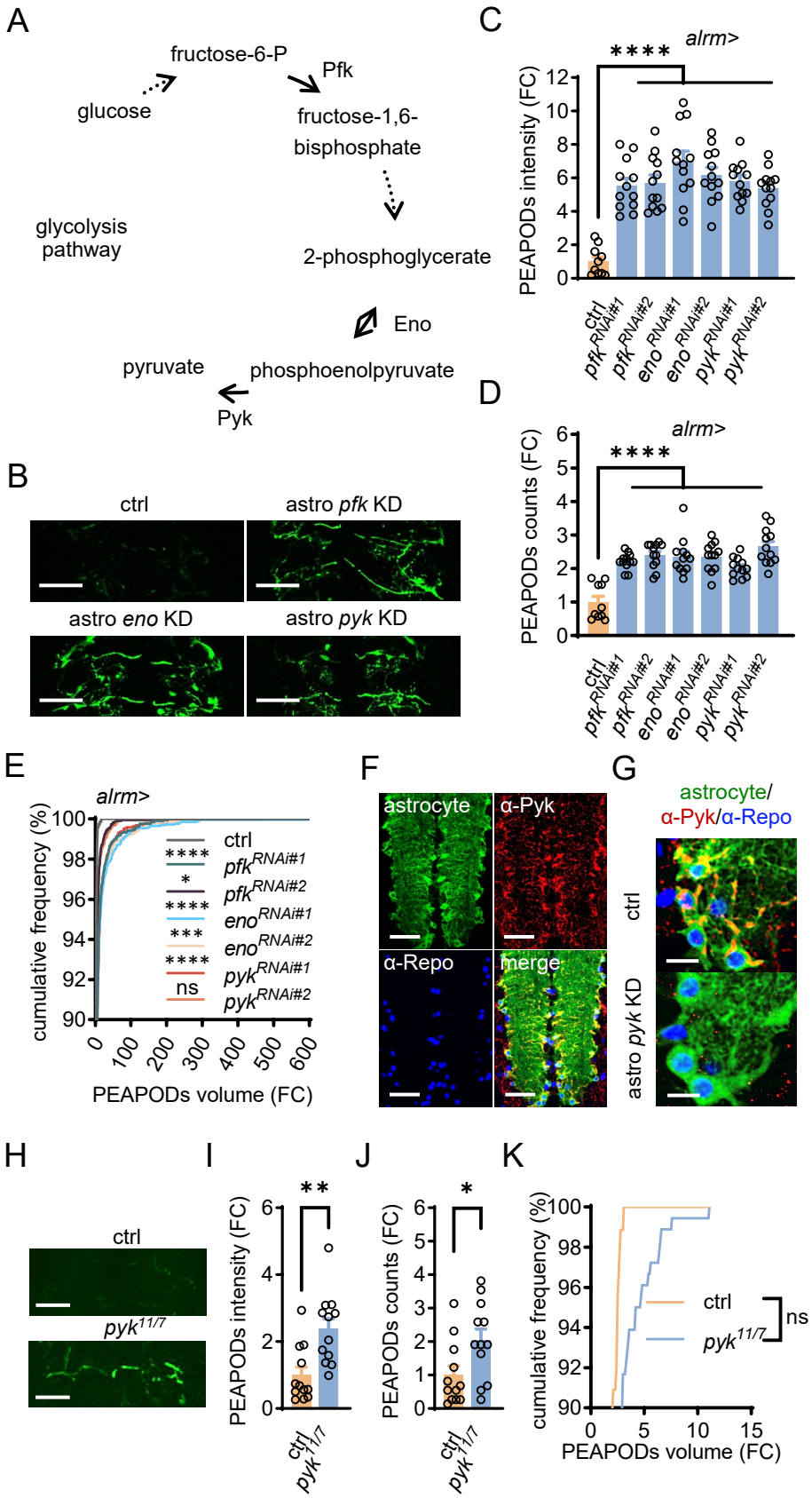
A
fructose-6-P
Pfk
glucose
fructose-1,6-bisphosphate
glycolysis pathway
2-phosphoglycerate
Eno
pyruvate
phosphoenolpyruvate
Pyk
B
ctrl
astro pfk KD
astro eno KD
astro pyk KD
C
alrm>
****
PEAPODs intensity (FC)
ctrl
pfk RNAi#1
pfk RNAi#2
eno RNAi#1
eno RNAi#2
pyk RNAi#1
pyk RNAi#2
D
alrm>
****
PEAPODs counts (FC)
E
alrm>
cumulative frequency (%)
ctrl
pfk RNAi#1
pfk RNAi#2
eno RNAi#1
eno RNAi#2
pyk RNAi#1
pyk RNAi#2
****
*
****
***
****
ns
PEAPODs volume (FC)
F
astrocyte
α-Pyk
α-Repo
merge
G
astrocyte/
α-Pyk/α-Repo
ctrl
astro pyk KD
H
ctrl
pyk11/7
I
**
PEAPODs intensity (FC)
ctrl
pyk11/7
J
*
PEAPODs counts (FC)
ctrl
pyk11/7
K
cumulative frequency (%)
ctrl
pyk11/7
ns
PEAPODs volume (FC)

Fig. 2

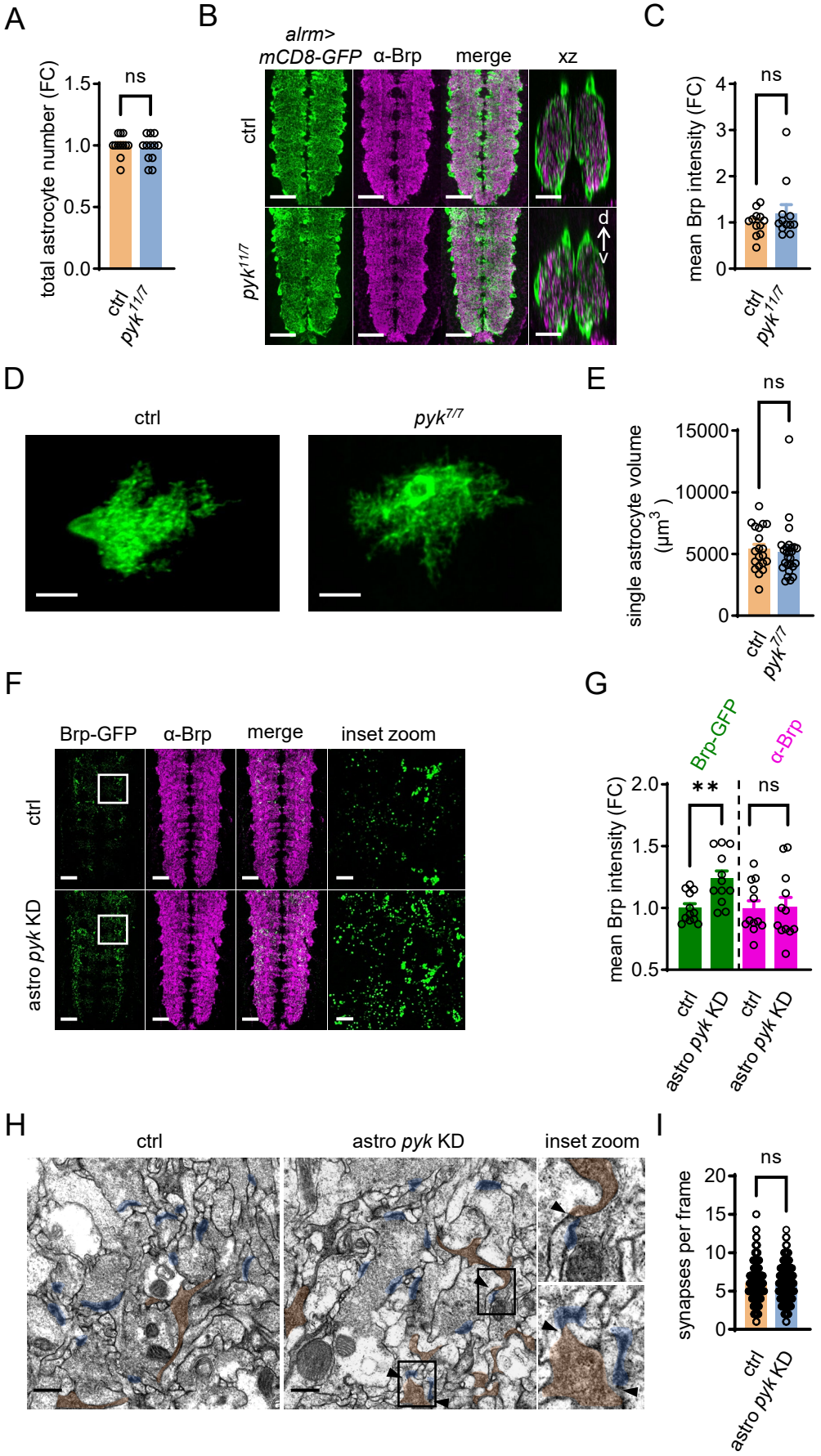
A
total astrocyte number (FC)
1.5
1.0
0.5
0.0
ns
ctrl
pyk11/7
B
alrm>
mCD8-GFP
α-Brp
merge
xz
ctrl
pyk11/7
d
v
C
mean Brp intensity (FC)
4
3
2
1
0
ns
ctrl
pyk11/7
D
ctrl
pyk7/7
E
single astrocyte volume
(μm3)
15000
10000
5000
0
ns
ctrl
pyk7/7
F
Brp-GFP
α-Brp
merge
inset zoom
ctrl
astro pyk KD
G
Brp-GFP
α-Brp
mean Brp intensity (FC)
2.0
1.5
1.0
0.5
**
ns
ctrl
astro pyk KD
ctrl
astro pyk KD
H
ctrl
astro pyk KD
inset zoom
I
synapses per frame
20
15
10
5
0
ns
ctrl
astro pyk KD

Fig. 3

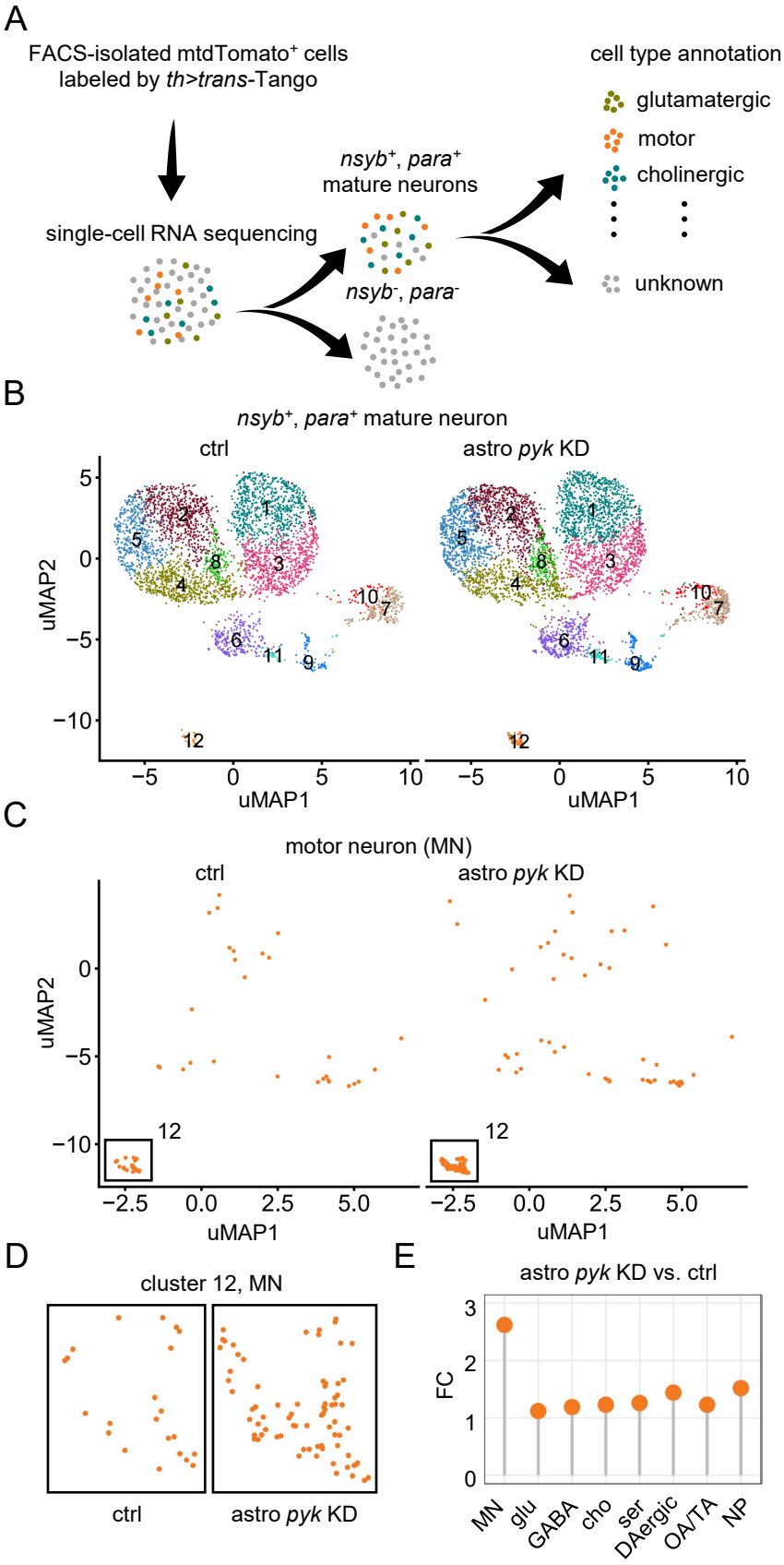
A
FACS-isolated mtdTomato+ cells
labeled by th>trans-Tango
single-cell RNA sequencing
nsyb+, para+
mature neurons
nsyb-, para-
cell type annotation
glutamatergic
motor
cholinergic
unknown
B
nsyb+, para+ mature neuron
ctrl
astro pyk KD
uMAP2
uMAP1
C
motor neuron (MN)
ctrl
astro pyk KD
uMAP2
uMAP1
D
cluster 12, MN
ctrl
astro pyk KD
E
astro pyk KD vs. ctrl
FC
MN
glu
GABA
cho
ser
DAergic
OA/TA
NP

Fig. 4

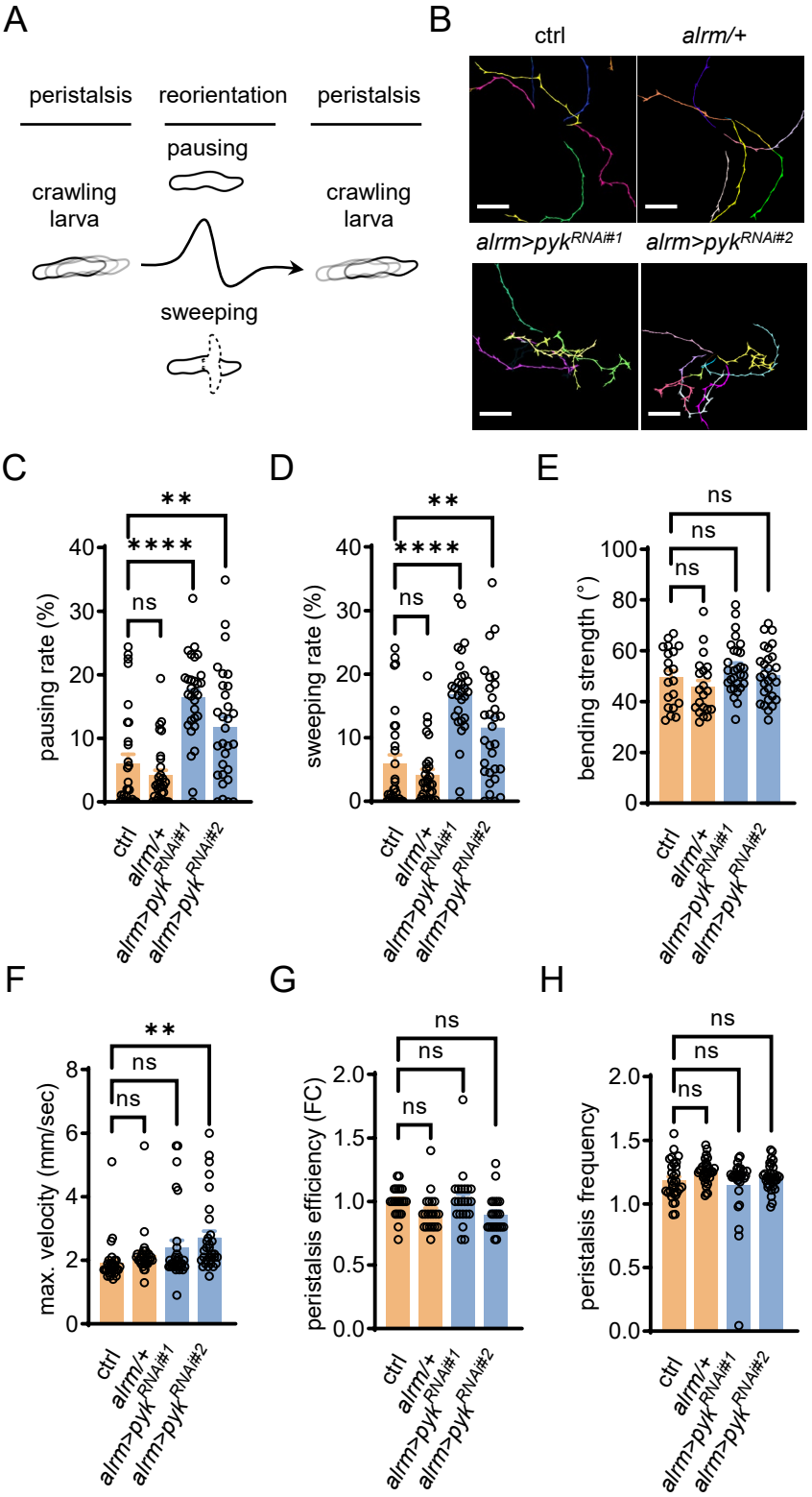
A
peristalsis
reorientation
peristalsis
pausing
crawling larva
crawling larva
sweeping
B
ctrl
alrm/+
alrm>pyk^RNAi#1
alrm>pyk^RNAi#2
C
pausing rate (%)
D
sweeping rate (%)
E
bending strength (°)
F
max. velocity (mm/sec)
G
peristalsis efficiency (FC)
H
peristalsis frequency
ctrl
alrm/+
alrm>pyk^RNAi#1
alrm>pyk^RNAi#2
ns
**
****

Fig. 5

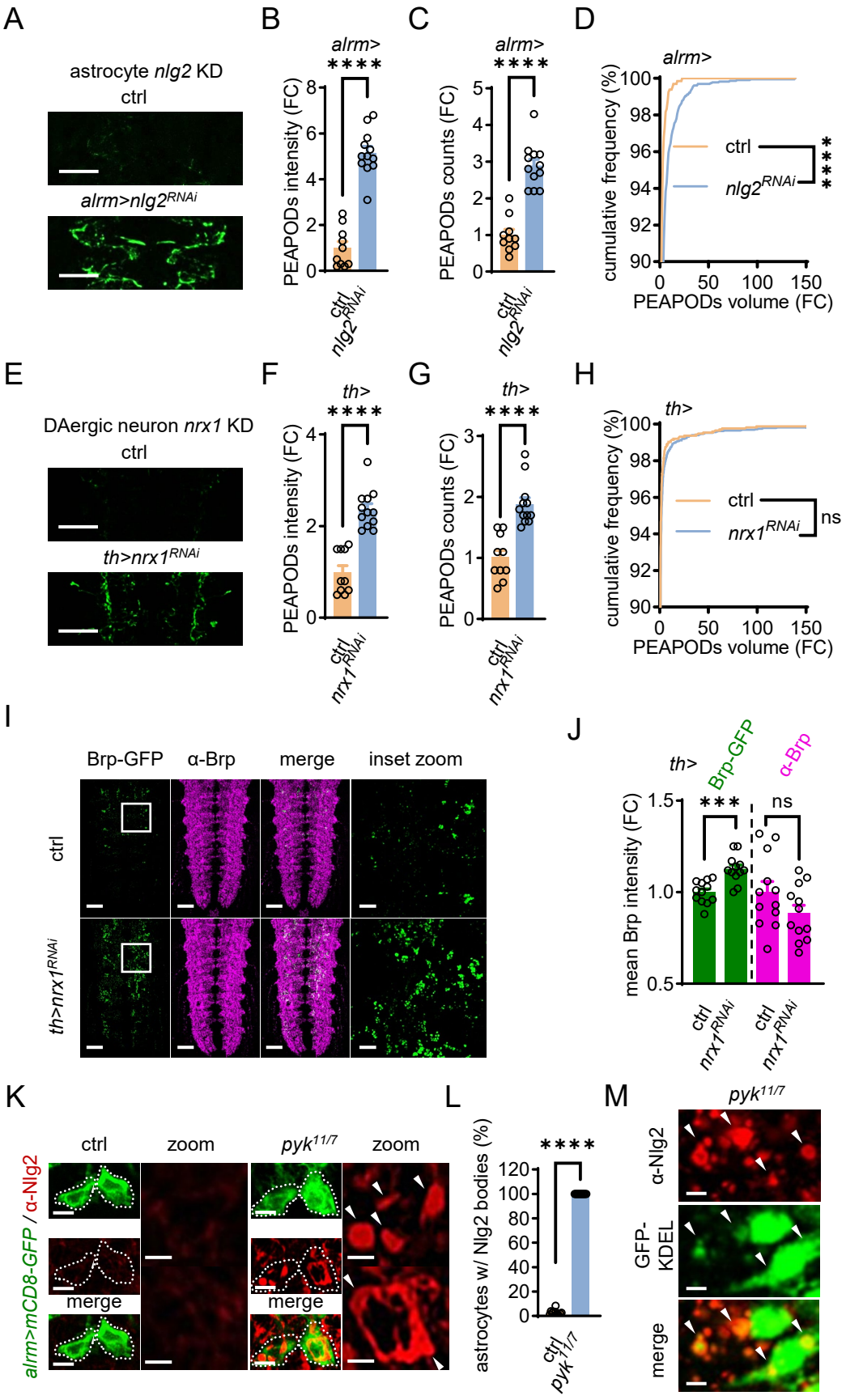
A
astrocyte nlg2 KD
ctrl
alrm>nlg2RNAi
B
alrm>
****
PEAPODs intensity (FC)
ctrl
nlg2RNAi
C
alrm>
****
PEAPODs counts (FC)
ctrl
nlg2RNAi
D
alrm>
cumulative frequency (%)
ctrl
nlg2RNAi
***
PEAPODs volume (FC)
E
DAergic neuron nrx1 KD
ctrl
th>nrx1RNAi
F
th>
****
PEAPODs intensity (FC)
ctrl
nrx1RNAi
G
th>
****
PEAPODs counts (FC)
ctrl
nrx1RNAi
H
th>
cumulative frequency (%)
ctrl
nrx1RNAi
ns
PEAPODs volume (FC)
I
Brp-GFP
α-Brp
merge
inset zoom
ctrl
th>nrx1RNAi
J
th>
Brp-GFP
α-Brp
***
ns
mean Brp intensity (FC)
ctrl
nrx1RNAi
ctrl
nrx1RNAi
K
ctrl
zoom
pyk11/7
zoom
alrm>mCD8-GFP / α-Nlg2
merge
merge
L
****
astrocytes w/ Nlg2 bodies (%)
ctrl
pyk11/7
M
pyk11/7
α-Nlg2
GFP-KDEL
merge

Fig. 6

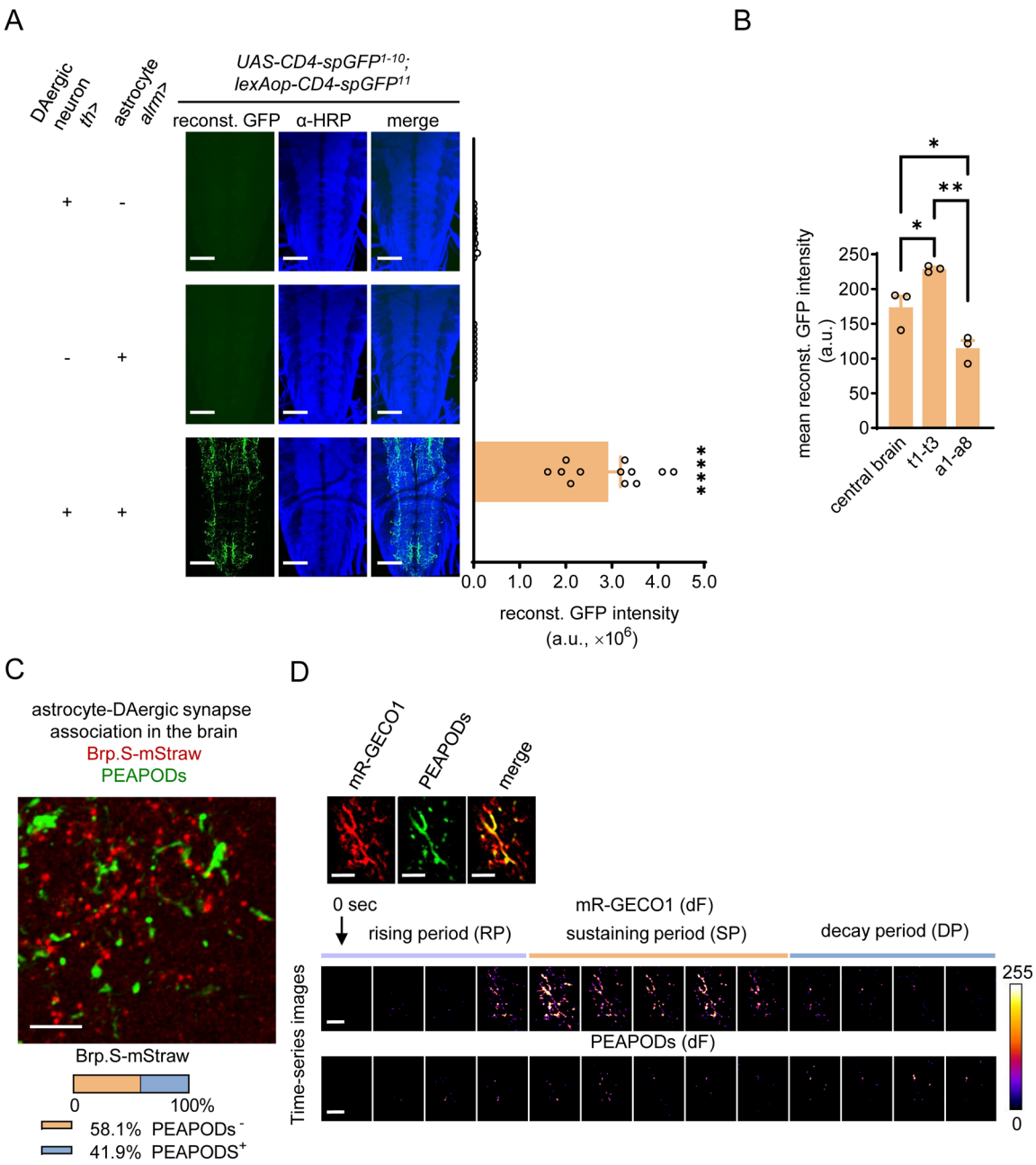

Fig. S1. Trans astrocyte-DAergic neuronal GFP reconstitution, and PEAPODs remodeling during spontaneous DAergic neuronal activation.

(A) Trans astrocyte-DAergic neuronal reconstituted GFP (reconst. GFP) (n = 12) (scale bars: 50 μm). α-HRP (horseradish peroxidase) stains neural tissues. The drivers *th-Gal4* (*th*) and *alrm-LexA* (*alrm*) were used here. a.u.: Arbitrary unit. (B) Regional variations in reconstituted GFP (reconst. GFP) intensity across the larval ventral nerve cord (VNC; thoracic segments, t1–t3; abdominal segments, a1–a8) and central brain (n = 3). a.u.: Arbitrary unit. (C) Single-cell PEAPODs and synaptic labeling of the DAergic neuron in larval brain (n = 10) (scale bars: 5 μm). (D) Dual-color live imaging of PEAPODs and spontaneous DAergic neuronal activation. Active DAergic neuronal projections (labeled by mR-GECO1) and their associated PEAPODs. Time-series dF (F_t–F_0) images show the differential fluorescence intensity at the time point of t second as compared to the baseline (0 s) (scale bars: 10 μm). Imaging time interval, 0.7 s.

One-way ANOVA with Tukey's test. *P < 0.05, **P < 0.01, ****P < 0.0001. FC: Fold change.

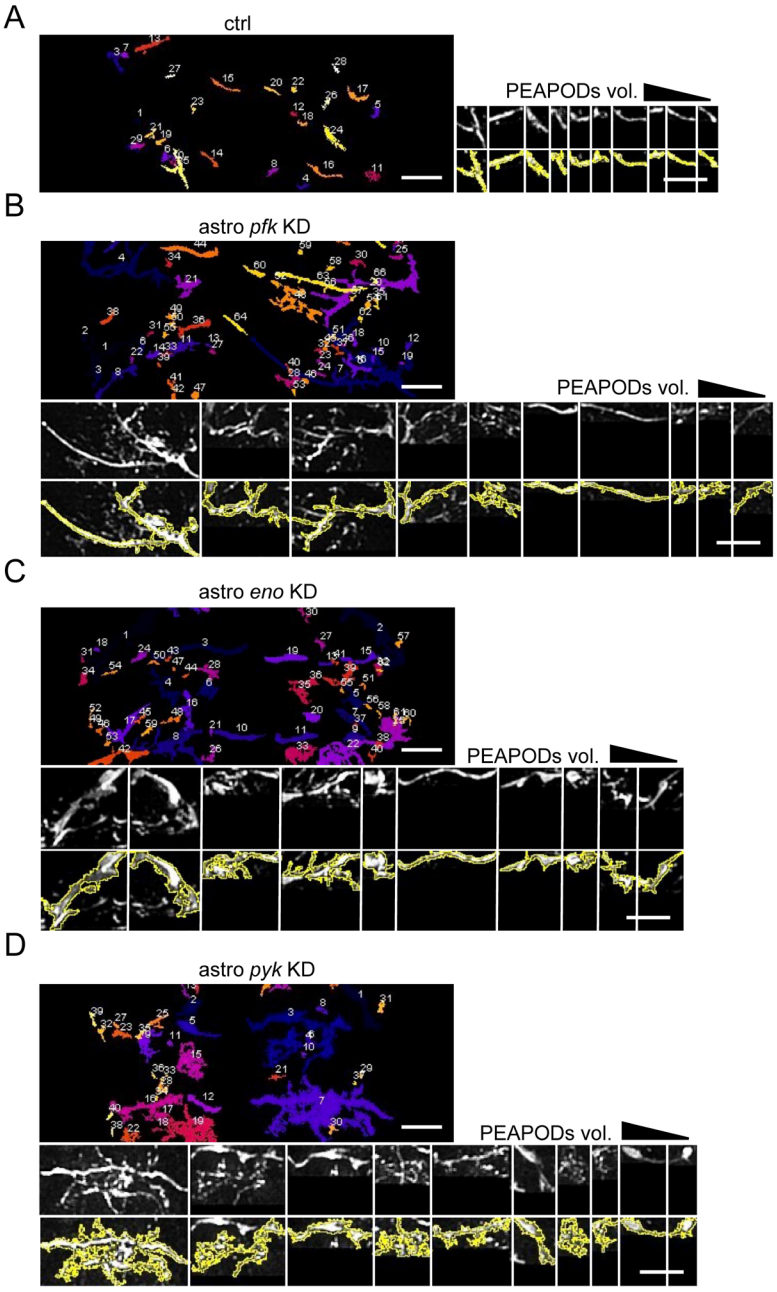

Fig. S2. The knockdown of glycolytic genes that stimulate PEAPODs.

(A–D) Three-dimensional segmentation and numbering of individual PEAPODs (scale bars: 25 μm). Ten largest PEAPODs from the indicated genotypes were sorted by volume (vol.), and they are delineated by the orange line (scale bars: 25 μm). astro: Astrocyte, KD: Knockdown.

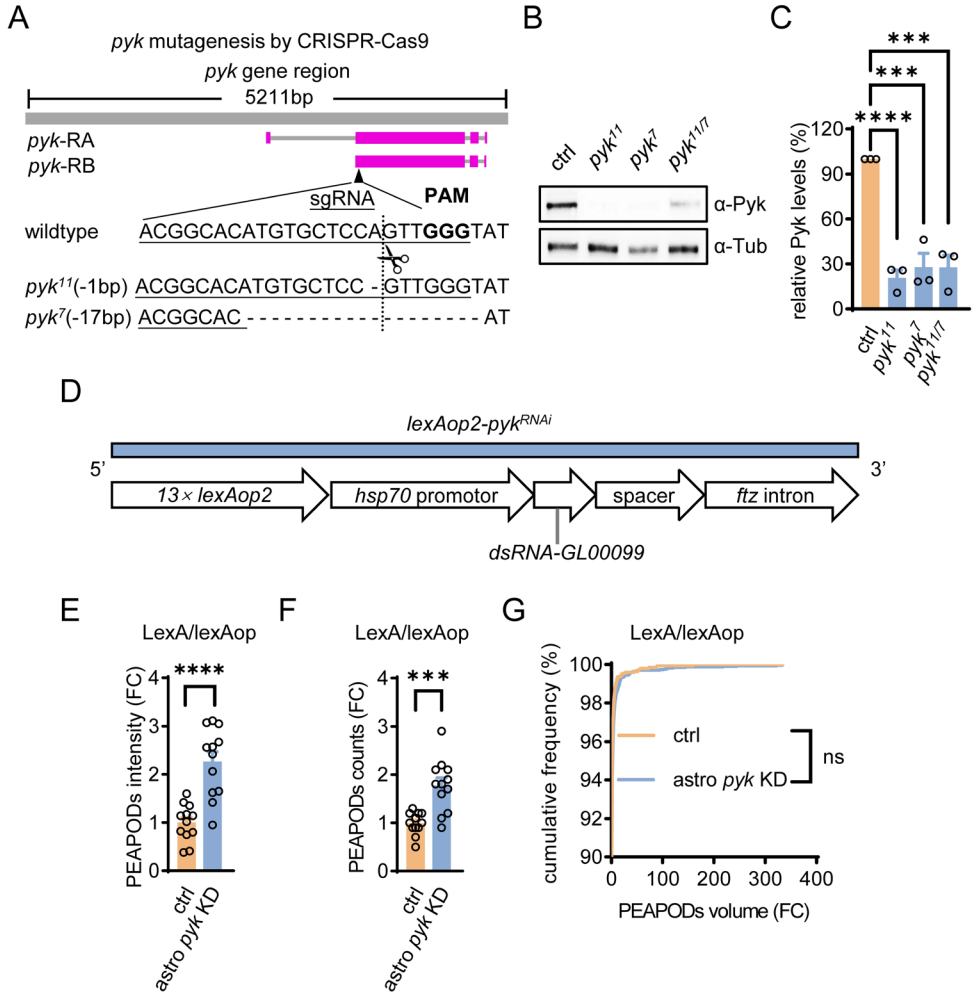

Fig. S3. *pyk* mutagenesis using CRISPR-Cas9, *lexAop2-pyk^{RNAi}* construct assembly.

(A) Schematics of the *pyk* gene region, two predicted transcripts (*pyk*-RA, -RB), short guide RNA (sgRNA) for guiding Cas9 to the *pyk* locus, and DNA lesions of the two mutated alleles, *pyk^{11}* and *pyk^{7}*. PAM: Protospacer adjacent motif. (B and C) Western blotting using α-Pyk antibody (B), and quantitated relative Pyk protein levels (C). Loading control, α-Tub (tubulin). Genotypes as indicated (n = 3). (D) Schematic illustration of *lexAop2-pyk^{RNAi}* construct assembly. *dsRNA-GL00099* is the TRiP RNAi amplicon (used in *pyk* RNAi line #1) for generating short hairpin RNA (shRNA) targeting *pyk*. The *ftz* intron was purposed to facilitate shRNA nuclear export. The illustrated elements (DNA sequence included in Table S3) arranged as such were cloned into the *pUASTattB* backbone. Note that *5× UAS* was replaced by 13 copies of *lexAop2* in tandem (*13× lexAop2*). (E–G) PEAPODs abundance analysis. Astrocyte (astro) *pyk* knockdown (KD) using LexA/lexAop system. Genotypes as indicated (n = 12; in G, 1970–3519 individual PEAPODs in total).

(C), one-way ANOVA with Tukey's test. (E), (F), unpaired t-test. (G), Kolmogorov-Smirnov test. ***$P < 0.001$, ****$P < 0.0001$. ns: Not significant, FC: Fold change.

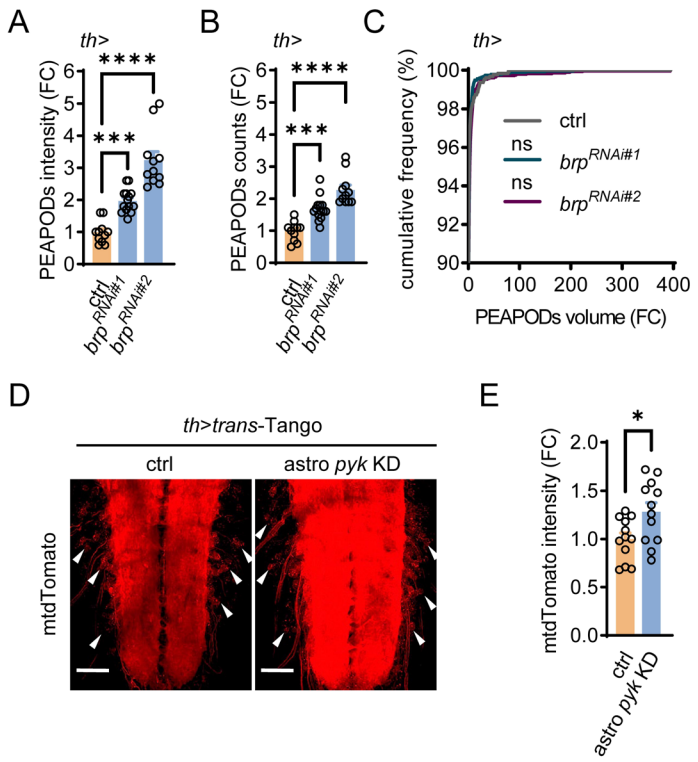

Fig. S4. PEAPODs in DAergic neuron *brp* knockdown (KD) transsynaptic (DAergic synapse) tracing by *trans*-Tango.

(A–C) PEAPODs abundance analysis. Genotypes as indicated (n = 11–14; in C, 1267–2876 individual PEAPODs in total). *th*: DAergic neuron driver. (D and E) mtdTomato intensity. The postsynaptic partners of DAergic neurons express myristoylated tdTomato (mtdTomato) (scale bars: 50 μm). Arrowheads denote the neuron somata. Genotypes as indicated (n = 12). *trans*-Tango: Transsynaptic labeling system, astro: Astrocyte, KD: Knockdown.

(A), (B), one-way ANOVA with Tukey's test. (C), Kolmogorov-Smirnov test. (E), unpaired t-test. *$P < 0.05$, ***$P < 0.001$, ****$P < 0.0001$. ns: Not significant, FC: Fold change.

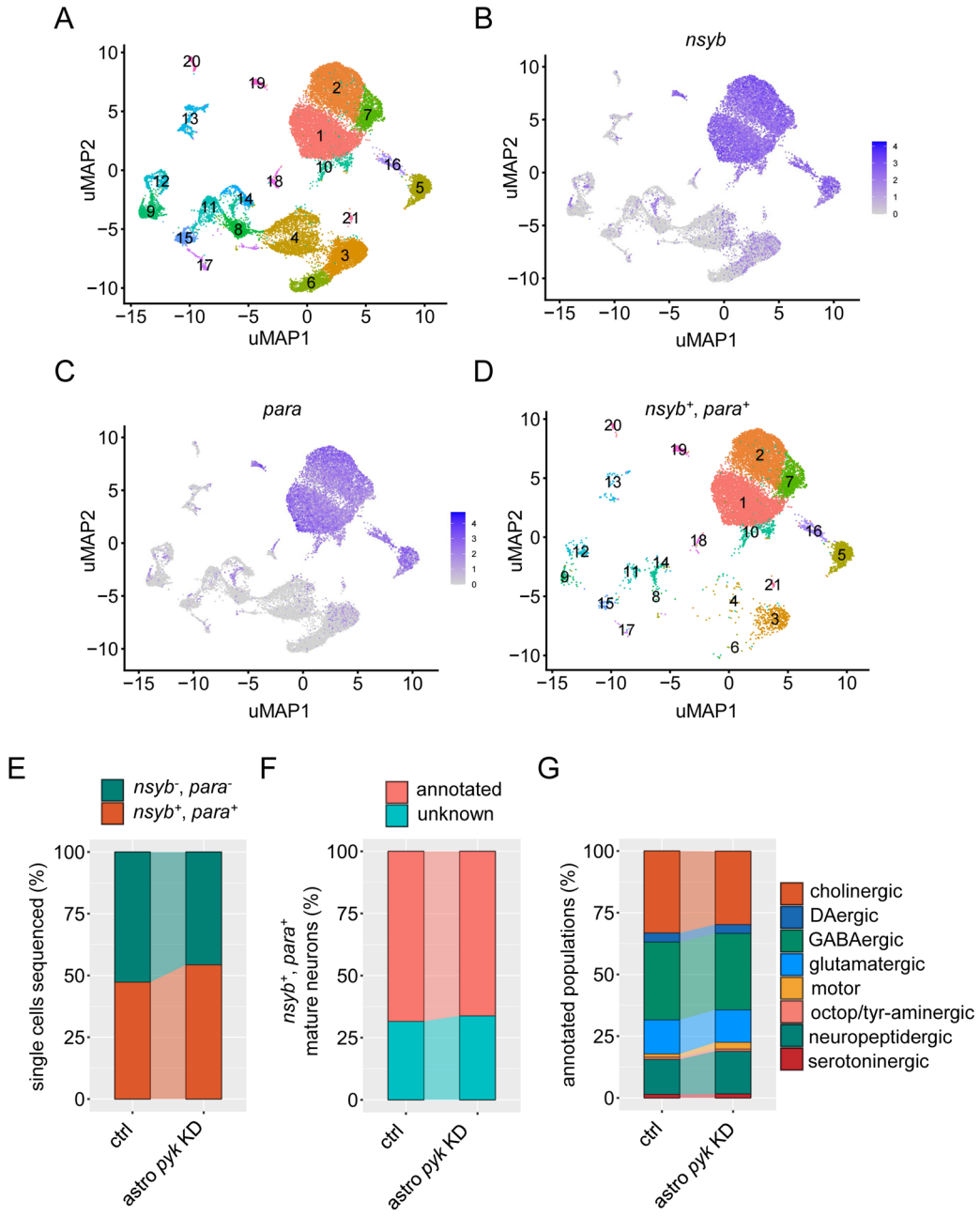

Fig. S5. scRNA-seq and cell type annotation of postsynaptic partners connected to DAergic neurons.

(A) Integrated clustering of all cells sequenced from ctrl (n = 11815) and astrocyte (astro) *pyk* knockdown (KD) (n = 13327) in uMAP. uMAP: Uniform manifold approximation and projection. (B and C) Single cells expressing *nsyb* (B), *para* (C). Note that the cells showed a tendency to converge in the upper right groups, e.g., clusters 1, 2, 5, 7, 10, 16, and 19. Color scale: Normalized gene expression level. (D) Highlighted *nsyb*$^+$*para*$^+$ cells in clusters. (E) Percentages of *nsyb*$^-$*para*$^-$ cells and *nsyb*$^+$*para*$^+$ mature neurons in all sequenced cells. (F) Percentages of (un)annotated neurons in mature neurons. (G) Percentages of defined populations in annotated mature neurons.

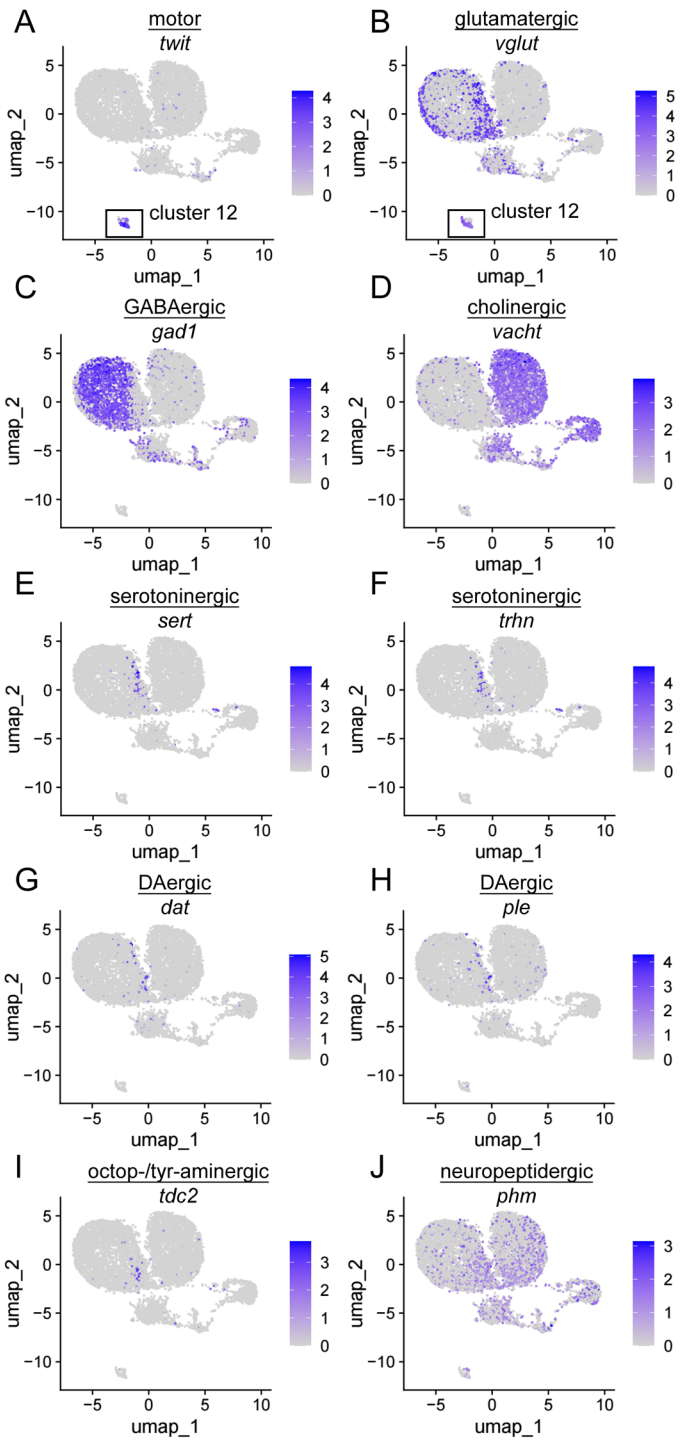

Figure S6. Annotated populations defined by unique marker genes.

(A and B) Motor neuron (MN) and marker gene *twit* (A). Glutamatergic neuron and marker gene *vglut* (B). Note that MNs gathered in cluster 12, which was also *vglut*$^{+}$. (C) GABAergic neuron and marker gene *gad1*. (D) Cholinergic neuron and marker gene *vacht*. (E and F) Serotoninergic neuron and marker genes: *sert* (E), *trhn* (F). (G and H) DAergic neuron and marker genes: *dat* (G), *ple* (H). (I) Octop-/tyr-aminergic neuron and marker gene: *tdc2*. (J) Neuropeptidergic neuron and marker gene: *phm*.
Integrated clustering contains all annotated cells from the ctrl and astrocyte *pyk* knockdown. uMAP: Uniform manifold approximation and projection, color scale: Normalized gene expression level.